Electrical Engineering Department

UNIVERSITY OF MARYLAND, COLLEGE PARK, MD 20742

Research Grant NAG 5 1383

Development of Simplified External Control Techniques for Broad Area Semiconductor Lasers

Final Report to:

National Aeronautics and Space Administration
Instrument Division
Engineering Directorate
Goddard Space Flight Center
Greenbelt, MD 20771

Principal Investigator
Christopher C. Davis
Electrical Engineering Department
University of Maryland
College Park
Maryland 20742
(301)454-6847

Date: February, 1993

COLLEGE OF ENGINEERING: GLENN L. MARTIN INSTITUTE OF TECHNOLOGY

Research Grant NAG 5 1383

Development of Simplified External Control Techniques for Broad Area Semiconductor Lasers

Final Report to:

National Aeronautics and Space Administration
Instrument Division
Engineering Directorate
Goddard Space Flight Center
Greenbelt, MD 20771

Principal Investigator
Christopher C. Davis
Electrical Engineering Department
University of Maryland
College Park
Maryland 20742
(301)454-6847

Date: February, 1993

SUMMARY

The goal of this project was to injection lock a 500mW broad area laser diode (BAL) with a single mode low power laser diode with injection beam delivery through a single mode optical fiber (SMF). This task was completed successfully with the following significant accomplishments:

- Injection locking of a BAL through a single-mode fiber using a master oscillator and integrated miniature optics.
- Generation of a single-lobed, high-power far-field pattern from the injection-locked BAL that steers with drive current.
- A comprehensive theoretical analysis of a model that describes the observed behavior of the injection locked oscillator.

This work has lead to the publication of a NASA Tech Brief:
Geoffrey Hazel, Patricia Mead, Christopher Davis, and Donald Cornwell, "Broad-Area Laser Diode with Fiber-Optic Injection," NASA Tech Briefs, 16,24, 1992
a presentation at LEOS '91:
G. Hazel, P. Mead, D. Cornwell, and C.C. Davis, "Fiber Injection Locked Broad Area Laser Diode," post-deadline paper presented at the Annual Meeting of the Lasers and Electro-Optics Society, San Jose, California, November 4-7, 1991.
and a manuscript in preparation for the IEEE Journal of Quantum Electronics.

Personnel

The people who have contributed to this work include:
Christopher C. Davis, Professor of Electrical Engineering
Patricia Mead, Ph.D. student in Electrical Engineering
Geoff Hazel, M.S. student in Electrical Engineering
Dr. Simon P. Bush, research associate in Electrical Engineering
Donald M. Cornwell of NASA GSFC was also a major contributor to the project. During the time of the contract he received his M.S. degree in Electrical Engineering from the University of Maryland, College Park Mr. Cornwell's thesis was entitled:
"Modulation Characteristics of a High-Power Semiconductor Master Oscillator Power Amplifier."
Mr. Cornwell, together with Geoffrey Hazel, Ms. Pat Mead and Professor Davis received a NASA Certificate of Recognition for the creative development of a technical innovation for their work on the injection locked BAL. Geoffrey Hazel also received his M.S. degree for his contributions to the BAL injection locking project. His thesis was entitled:
"Numerical and Experimental Analysis of High Power Semiconductor Master Oscillator-Power Amplifier Systems."

This M.S. thesis written by Geoffrey Hazel represents a comprehensive discussion of both our experimental work in studying injection locking of BALs and Mr. Hazel's major contribution involving a theoretical analysis of a model that describes the observed behavior of the injection locked BAL. The final report that follows contains substantial parts of Mr. Hazel's thesis.

INTRODUCTION

The development of semiconductor laser diodes has opened a broad new field of laser research with the promise of significant improvements over other types of lasers along with many new practical applications. The most important features of semiconductor lasers are their small size and high efficiency. Typical semiconductor lasers can be 30% or more efficient as compared to most gas, solid state, dye or excimer lasers whose efficiencies are frequently less than 1%. Semiconductor lasers are very small: the devices themselves are measured in micrometers or hundreds of micrometers and they and their drive electronics can be fabricated on a single integrated circuit [1].

Because of these features semiconductor lasers have found many applications and are being considered for many more. For example, they are the key sources in non-coherent optical fiber communication systems and show promise as sources for coherent and free space communication links. They are used in laser printers, photocopiers and compact disc players. Semiconductor lasers have also proved to be effective pump sources for other solid state lasers, especially Nd:YAG lasers. Laser ranging, altimetry and Laser RADAR are also applications for which semiconductor lasers are being investigated.

Semiconductor lasers have been employed most successfully in relatively low power applications such as long and short haul fiber optic communication links and compact discs. Unfortunately, higher power devices begin to display disadvantageous behavior. Compact, efficient semiconductor lasers do exist that operate at very high power levels (up to 20W CW and 60W Quasi-CW [2]) but they operate in multiple spectral modes and produce high divergence, non-diffraction limited output beams. Applications such as laser RADAR, ranging and altimetry and free space communication require high power sources with good spectral and spatial coherence.

One important technique that produces a source with these qualities from semiconductor lasers is the Master Oscillator-Power Amplifier (MOPA) technique. In this arrangement the diffraction limited beam of a low power, single mode laser diode is focused into the facet of a high power multimode laser diode array or broad area laser. The high power device can then be made to emit a narrow, near-diffraction-limited output beam with the same spectral characteristics as the low power device. The result is a source with the spatial and spectral coherence properties required for the applications noted above.

This scheme can be viewed as either an injection locked oscillator or as a simple regenerative amplifier. When the phenomenon was first observed experimentally it was attributed to injection locking, a mode of operation well known in electrical oscillators and other systems [3,4,5,6,7,8,9]. The first theoretical models of this behavior attributed it to the coherent coupling of several laser cavity modes frequency locked by the injected light [10,11,12,13,14,15]. While these models did predict the single lobed, narrow frequency output of the injection locked system, they had difficulty predicting other aspects of the system's behavior. In addition, these coupled mode theories were mathematically cumbersome and yielded little physical insight.

ore recently models that treat this system as regenerative amplification of a low power oscillator signal have been widely adopted [16,17,18,19,20,21,22,23]. This MOPA description

can explain much of the system's behavior and has the advantage of relative simplicity. Recent experimental efforts have focused on broad area devices with anti-reflection coated facets, and hence high self oscillation thresholds, which operate in single or double pass traveling wave amplifier configurations [24,25,26,27]. Such devices have been reported to produce as much as 3W of quasi-CW power in a narrow spectrum, diffraction limited beam [28].

A major drawback to MOPA schemes is the increased complexity and size of the complete system. A MOPA must consist of two active devices, oscillator and amplifier, and some sort of passive optical system to deliver light to the amplifier and decouple this light from the amplifier output. This optical system also introduces alignment sensitivity and coupling losses that reduce the overall system efficiency. There are several approaches under investigation to alleviate these problems, one of which will be examined here.

The work described here is in three parts. First, the construction and experimental study of a MOPA using fiber optic master oscillator coupling is described. Second, two existing numerical models based on the MOPA approach are developed and compared with each other and the experimental data. Third a simple numerical model of the spontaneous emission in a semiconductor traveling wave amplifier is developed.

Fiber optic master oscillator coupling has been proposed to reduce the size, complexity, and alignment sensitivity of MOPA systems. In what follows, a fiber coupled MOPA design will be presented along with a characterization of its performance. From this work some conclusions will be drawn regarding the feasibility of fiber coupled MOPAs.

The first numerical model to be developed is the regenerative Gaussian beam amplifier (RGBA) model [17]. This is a particularly simple model that qualitatively predicts the regenerative effects in a MOPA caused by interference between multiple passes of the amplified signal through the gain region. However, it neglects any effects of non-uniform gain saturation. The second model uses a spectral beam propagation method to solve self-consistently for the gain and field distributions in the amplifier and gives more quantitative results [16]. This model, however, neglects regenerative effects by assuming negligible amplifier facet reflectivity. This assumption is more realistic for recent experimental work with low reflectivity traveling wave amplifiers.

The spontaneous emission model takes a simple approach by considering only the emission at the master oscillator wavelength, which is assumed to be at the center of the amplifier gain curve. The model is valid for single or double pass traveling wave amplifiers that are longer than they are wide. Despite its simple nature, this model provides predictions in better agreement with experimental data than previous models which neglect saturation effects due to amplified spontaneous emission (ASE).

1. BACKGROUND
REVIEW OF PREVIOUS EXPERIMENTAL RESULTS

Early Laser Injection Locking Studies

The first observation of the injection locking of two laser oscillators was reported by Stover and Steier in 1966 [8]. The two oscillators used in this experiment were both acoustically shielded single mode Helium–Neon lasers operating at 6238 Å which were tuned by a piezoelectric-transducer-mounted cavity mirror. The two lasers were coupled through an optical isolator and their outputs were combined at the input of a photomultiplier tube. Injection locking was observed by monitoring the interference between the two beams. As the frequency of one laser was swept, phase locking was observed over a locking bandwidth that varied with injected power.

Injection locking of single mode AlGaAs semiconductor lasers was reported in a similar study by Kobayashi and Kimura in 1981 [3]. In this experiment the two oscillators were again coupled through an optical isolator and their interference pattern and mode spectra were monitored. The master laser was current tuned and the locking bandwidth was measured as a function of injected power. The variation of the locking bandwidth was found to agree with the prediction of the classic paper on locking phenomena by Adler [9]. The power gain of the locked output over the injected input was also measured in this study and was found to have a maximum value of 40dB for a small injected signal.

There were also a number of reported studies of hybrid injection locking systems in which a semiconductor laser was injection locked by some other type of master laser. For example, Wyatt, et. al. [7] reported using a Helium–Neon laser operating at 1.523 μm to injection lock and reduce the spectrum of a 1.5 μm semiconductor laser from a multimode spectrum of more than 1 GHz to a single mode with a linewidth below their 1.5 MHz measurement resolution. In another experiment Hohimer, et. al. used a dye laser to injection lock a 100mW laser diode array [6]. This report demonstrated the production of a single lobed near-diffraction-limited far-field pattern as well as single spectral mode operation of the laser diode array. Hybrid injection locking or MOPA systems are also being studied in current work such as the dramatic 12 W semiconductor amplifier reported by Goldberg, et. al. in which the amplified signal was from a Ti:sapphire laser.

Single Mode Semiconductor Laser Amplifiers

Another important area of research leading up to current MOPA systems concentrated on developing single mode semiconductor laser amplifiers [22,23,26,29-32]. The motivation for this work is to produce a simple linear optical gain block analogous to an electrical Op-Amp. Such a device could be used to compensate for coupling and splitting losses in optical logic, processing, and communications networks or to act as a linear repeater in a fiber optic communication link or as a receiver preamplifier to improve detection sensitivity. An early example of this work is the paper by Yamamoto in which the signal gain, saturation power, and noise bandwidth of a single mode AlGaAs laser amplifier were measured [29].

An important point about single mode diode laser amplifiers is that the requirement of linearity implies that the device must operate in the relatively low power regime in which

the gain medium remains unsaturated. As a result, the single pass gain of the device remains near its high small signal value. As we will see in a later section, high single pass gain in a laser amplifier with residual facet reflection causes undesirable Fabry-Perot ripples in the amplifier frequency response unless the facet reflectivity can be made very small. For this reason, recent research efforts on single mode diode laser amplifiers has concentrated on the development of good, reliable, anti-reflection coating techniques for laser diode facets. While intensive research on single mode diode lasers is still underway, the limitations outlined above have led researchers looking for high power optical amplifiers to turn to larger multimode diode arrays and broad area lasers (BALs) which operate in the highly saturated regime [25].

Development of High Power Multi-Mode MOPAs

Since MOPA systems based on large multi-mode laser diodes can be operated at high powers beyond the linear gain region where the gain medium is highly saturated, their single pass cavity gain can be much less than the unsaturated value. This relaxes the requirements on facet coating quality necessary for an acceptably flat frequency response. However, recent high power MOPA experiments continue to use the best available anti-reflection coatings to reduce injected beam coupling losses and to prevent amplifier self-oscillation [24,25]. The first report of the injection locking of a high power laser diode array was by Goldberg, et. al. in 1985 [5]. In this experiment a 105mW 10-element laser diode array was injected off-axis with light from a single mode AlGaAs laser diode. The resulting far-field pattern contained a 0.5° wide off-axis main lobe that included 60–70% of the 105mW array output power.

Similar experiments have been reported since that use increasingly large, powerful laser diode arrays and BALs (see Table (1)) [4,25,33,34]. Most recently, 12W peak pulsed power in a diffraction-limited lobe has been reported using a 600 μm wide by 1000 μm long GaAlAs BAL to amplify an injected signal from a Ti:sapphire laser [24]. In addition, a similar recent experiment produced 3W of quasi-cw power from the same amplifier using a single mode semiconductor laser as a master oscillator [28].

Detailed MOPA Studies and Related Work

An important feature of multi-mode MOPA systems is that when the multi-mode device is injected with master oscillator power, both the spectral properties and the spatial detail of the output radiation are affected. The investigation and characterization of these two effects has been studied extensively in a variety of MOPA devices. In 1988 Abbas, et. al. described a set of spectrally resolved measurements of the near-field and far-field profiles of the output of a 100mW BAL injection locked by a single mode laser diode [17]. Spectrally resolved measurements allowed the amplified master oscillator radiation to be distinguished from the free running BAL radiation. This study characterized the effects of injection beam shape, injection angle and injection beam frequency tuning on the spatial detail of the BAL output. A simple saturated amplifier model, the Regenerative Gaussian Beam Amplifier (RGBA) model, which will be studied in detail in section 3, was also proposed and provided excellent agreement with the measurements.

Recently, Cornwell, et. al. studied the phase front aberration of the injection locked output of a AlGaAs diode array [35]. In this experiment a Mach-Zehnder interferometer

Table (1) Summary of Previous Injection Locking and MOPA Experiments

Year	Author	Size (μm^2)	Power	Comments
'81	Kobayashi	—	20 mW	Single mode diodes
'82	Wyatt	—	0.75 mW	HeNe locks single mode diode
'85	Goldberg	10-stripe	68 mW	First injection locked array
'85	Hohimer	10-stripe	100 mW	Array locked by dye laser
'86	Goldberg	20-stripe	180 mW	19 dB gain over MO
'87	Goldberg	40-stripe	150 mW	Coupled into single mode fiber
'87	Abbas	100 X 200	80 mW	Spectrally resolved measurements
				RGBA model proposed
'88	Goldberg	160 X 250	450 mW	High power BAL
'91	Goldberg	400 X 500	2.5 W	Pulsed, Ti:Sapphire MO
'91	Goldberg	600 X 1000	12 W	Pulsed, Ti:Sapphire MO
'92	Goldberg	600 X 1000	3 W	Quasi-cw, diode MO

was used to measure the phase front of the array far-field. A root-mean-square phase error of $\lambda/27$ was measured in a far-field lobe containing 240 mW cw power in a single spectral mode. This phase error is comparable to the phase error from a single-stripe index-guided AlGaAs laser. In a related study, Andrews and Schuster measured the spatial coherence of a MOPA system output beam in terms of interference fringe visibility [36]. An AlGaAs BAL was injected with 70 mW of master oscillator power to produce a 342 mW output beam diverging at 1.02× the diffraction limit. The self-coherence of the amplifier output was 0.97 and the mutual coherence between the amplifier and the master oscillator was 0.96 (1.0 represents perfect coherence and 0.0 represents complete incoherence). These two studies confirm that the output of a MOPA system can be a high quality, low aberration, near-diffraction-limited beam.

In order to avoid near-field filamentation and far-field degradation in high power MOPA systems, the oscillator input beam must be injected at a small angle from the facet normal [16,21]. The resulting output beam is centered near the opposite angle. However, due to cavity resonance requirements in a regenerative amplifier, the actual angle of the output beam steers as a function of the round trip phase delay. Hence in a semiconductor MOPA the output angle can be steered by modulating the bias current of either the master oscillator or the power amplifier [37,38]. In 1987 Swanson, et. al. studied this beam steering phenomenon in a 10-stripe diode array as it might be applied to high-speed tracking and scanning systems [37]. It was found that the beam steering bandwidth was limited by the FM response of the modulated device. In a later study, Brewer demonstrated how beam steering could be suppressed by using a well collimated injection beam [39]. This avoids the pointing difficulties that beam steering would cause in a free space communication link.

A unique two-stage MOPA system was described in a letter by Pang, et. al. in 1990 [40]. This experiment used a single mode diode laser as a master oscillator to inject into the first of two 40-stripe diode laser arrays. The amplified beam was then recollimated and injected into the second array. The arrangement produced a maximum large signal output power of 500mW and a small signal gain of 25dB with 290mW output power.

Applications to Communication Systems

A great deal of research has been done on the application of MOPAs to communication systems. This research includes device modulation characterization as well as complete communication system experiments. An early paper by Kobayashi and Kimura studied phase modulation in injection locked single mode laser diodes [kobayashi]. In this work a cw master oscillator beam was injected into a direct current modulated single mode laser diode to produce optical phase modulation in the output beam. The phase modulation frequency response of the system was characterized for a range of locking bandwidths and injection and output powers. Phase modulation was achieved at 1 GHz for a locking bandwidth of 1.4 GHz.

Goldberg, et. al. published the results of a 1986 study of a frequency modulated injection locked laser diode array in which both the master oscillator and the array were current modulated [42]. Two phased locked sinusoidal oscillators were used to modulate the bias

current of the master oscillator and the ten-element array. The amplitudes and relative phase of the oscillators were adjusted so that the array remained injection locked over the full swing of its modulated bias current. This arrangement was used to measure the current-to-frequency modulation transfer function for the array from dc to 100MHz.

In 1991 Cornwell characterized the response of a high power BAL based MOPA system in which the master oscillator was current modulated [43]. The amplitude modulation characteristics of the system were measured as a function of the current modulation induced frequency detuning between master oscillator and amplifier. The MOPA system was used to generate 200 mW and 250mW optical square-wave pulses at 10 MHz and 250MHz.

Lidoyne reported an experiment in which an injection locked laser diode was used as the local oscillator in an optical homodyne receiver [44]. In this arrangement part of the incoming phase modulated optical signal was used to injection lock the local oscillator. The remainder of the signal was then homodyned with the injection locked local oscillator output. A 1.6 dB improvement in receiver sensitivity over a standard phase locked loop was estimated. Another unique demodulation experiment was reported by Nakajima [45]. Here a 140 Mb/s optical FSK signal was used to injection lock a semiconductor distributed feedback laser. The forward bias voltage of the laser was then monitored to detect the signal. A detector sensitivity of -25.9 dBm was reported for a bit error rate of 10^{-9}.

An early example of a complete communication system experiment using a high power MOPA system was reported by Lucente, et. al. in 1989. [46] The system studied used a single mode master laser which was current modulated to produce a 110 Mb/s optical FSK signal. This signal was injected into a 20-element laser diode array producing a modulated single lobed output beam with 310mW optical power. The signal was transmitted through 400m of polarization preserving fiber and then optically attenuated before entering an optical heterodyne receiver. For comparison the same arrangement was also tested with only the unamplified master oscillator. It was found that when the MOPA was attenuated to the same receiver input power as the master oscillator, it performed equally well with no penalty in bit error rate. A similar recent experiment by Livas, et. al. demonstrated 1 Gb/s DPSK modulation in a 120mW MOPA system using a 20-element laser diode array amplifier in a free space communication link [47].

REVIEW OF PREVIOUS THEORETICAL RESULTS

Injection Locking

The classic treatment of locking phenomena in oscillators was given by Adler in 1946 [9]. This treatment considered an electrical oscillator with a small, similar frequency signal impressed upon its output terminal. A differential equation was developed for the phase difference between the oscillator and the impressed signal as a function of time and the condition for a steady state solution to this equation was derived. It was found that for an impressed signal whose frequency lay within a locking bandwidth of the oscillator free-running frequency, the oscillator frequency would shift to coincide with that of the impressed signal thus establishing a fixed phase relationship between the two signals. The dependence of the locking bandwidth on the ratio of the impressed signal amplitude to the oscillator amplitude was also derived and found to be linear. Although the results were

developed for electrical oscillators, the derivation did not depend on any of the properties of the particular system and, in fact, proved to be quite general.

The application of injection locking to laser oscillators was a natural extension from its application to lower frequency oscillators. Pantell studied the effects of an external signal on a laser oscillator, including locking, in 1965, before it was observed experimentally [12]. This paper considered the behavior of a single mode oscillator with an external signal in both the locked and unlocked regimes and outlined the boundary between the two regimes. In 1967, after the Stover and Steier experiments [8], Tang and Statz [13] published a simple analysis of injection locking of a single mode laser which started with the wave equation and paralleled Adler's derivation [9]. The analysis demonstrated the conditions under which the locking bandwidth for a laser oscillator has the same dependence on signal strengths and oscillator parameters as it does in the Adler development. In both of the above analyses it was seen that the key physical mechanism behind injection locking in a laser is the gain saturation induced by the small injected signal after it has been regeneratively amplified in the laser cavity. Locking is achieved when the saturation is strong enough to quench the natural laser oscillation.

Analysis of the complex interaction of injection locking and mode competition in a multi-mode laser oscillator came somewhat later. Ibrahim analyzed injection locking in a two mode homogeneously broadened laser in 1978 [48]. Then in 1983 Chow considered the case were a broad-band, multi-mode laser oscillator was injected with a signal of bandwidth much smaller than the longitudinal mode spacing [15]. Here the multi-mode semiclassical laser rate equation theory was applied to study the injection locking of the single mode nearest in frequency to the injected signal. Both homogeneously broadened and inhomogeneously broadened steady state laser oscillators were analyzed. The next step in the development of injection locking theory, the locking of multiple closely spaced oscillator modes by an injected signal, became important when injection locking was applied to multi-mode semiconductor lasers. Before this could be done an understanding of the mode structure of high power semiconductor laser oscillators needed to be established.

Semiconductor Diode Laser Cavity Modes

The natural resonant modes of a coupled stripe diode laser array cavity have been found by two analytical approaches both based on coupled mode theory. The first, array supermode theory, treats the array as a collection of weakly coupled, but otherwise independent single stripe lasers. The second, coupled broad area mode theory, treats the array as a single broad area waveguide whose modes are coupled by the periodic gain perturbation and by the temperature profile in the active layer. Otsuka first developed array supermode theory with the simplification that the number of stripes is very large [49]. In this approximation, supermode theory yields the same result as a diffraction theory treatment of the array as a collection of independent sources. In particular, only two modes are predicted: one with the fields in adjacent elements in phase resulting in a single lobed far-field, and the other with the fields 180° out of phase producing a double lobed far-field.

Butler, et. al., were the first to publish a supermode analysis of an N-element laser diode array [50]. Parallel efforts were developed independently by Kapon, et al., and

others [51,52]. The primary prediction of the supermode theory is the existence of exactly N allowed eigenmodes for an N-element array with the lowest and highest order modes corresponding to the in-phase and out-of-phase modes of the infinite-element coupled mode theory of Otsuka. The theory also predicts a separation of the two far-field lobes that increases with increasing mode number.

Array supermode theory agrees with the experimental data much more closely than a simple summation over independent oscillators and the existence of more than two oscillation modes was soon verified by experiment [53]. However, while supermode theory predicts the behavior of index-guided laser diode arrays reasonably well, it soon became apparent that it was not an adequate theory for describing gain-guided arrays. Through detailed experimental studies using external cavities, injection locking and spectrally resolved intensity profile measurements, oscillation modes were detected in diode arrays that supermode theory fails to predict [53-55]. In particular, these measurements exposed modes of order greater than the number of array elements. The higher order modes exhibited more peaks in the near-field and wider lobe separation in the far-field than the lower order modes predicted by supermode theory. The reason array supermode theory fails for gain-guided arrays is that it employs a perturbation approach that assumes only weak coupling between elements, while in reality the inter-element coupling can be quite strong. In fact, the experimental results mentioned above, among others, indicated that gain-guided arrays actually behave more like single broad area devices with a periodic lateral gain and index profile.

This observation led Verdiell and Frey to develop the coupled broad area mode approach to finding the eigenmodes of a gain-guided diode laser array [56]. This perturbation theory starts with the natural modes of a broad stripe laser cavity rather than the single modes of each of a collection of narrow stripe cavities. Two gain and index perturbations are then applied to couple the natural broad area modes into a new set of array eigenmodes. The first perturbation is the lateral periodic gain and index profile caused by the pumping stripes, the second is an assumed form of the lateral index profile induced by the temperature gradient inside the diode active layer. Once the modes are known the gain seen by each mode is also calculated. The result is a set of eigenmodes of unlimited number of which the highest gain mode is a mode of order greater than the number of array stripes. For a free running array in which the gain is clamped to threshold and gain and index saturation effects are small, the predictions of this theory agree very closely with both the experimental data as well as a detailed numerical model which will be discussed in the next section [57]. However, both coupled broad area mode theory and array supermode theory share one common fault, they both fail to self-consistently characterize the interaction between the cavity fields and the active region carriers.

Injection Locking of Laser Diode Eigenmodes

One approach to an analytical characterization of MOPA systems is to treat the MOPA fields as injection locked modes of the free running laser oscillator. This approach has been applied to both the array supermode theory and the coupled broad area mode theory. In the case of supermode theory, the presumed objective of injection locking is to preferentially select one of the array modes, typically the lowest order one, to oscillate over the

others. Chow, for example, analyzed an injection locked index-guided laser array in terms of supermode theory [10]. This paper considers a two element array and finds that a sufficiently intense injection field will force the array to operate in the lowest order supermode. The extension of this analysis to an N-element index-guided array is also discussed. Weber and Wang applied injection locked supermode theory to the N-element gain-guided array case [37]. The theory attempted to explain the angular steering of the locked far-field lobe with injected frequency. However, the explanation failed to capture the observed nearly continuous nature of the angular beam steering. The theory also made some other unobserved predictions about the injected array behavior under certain injection conditions. This is not surprising, however, in light of the previous discussion of the inappropriateness of supermode theory for gain-guided arrays.

Verdiell applied coupled broad area mode theory to the injection locking of gain-guided laser arrays in a 1991 paper [11]. Rather than selection of a particular mode, this approach treats the simultaneous injection locking of several of the more numerous coupled broad area modes. The predicted far-field pattern of the injection locked array is then taken to be a coherent sum of the far-field profiles corresponding to each of the locked modes. This model gives very good agreement with the experimental observations of injection locking in gain-guided arrays with low injected power. The nearly continuous nature of the beam steering is also better represented by more dense coupled broad area modes than by the array supermodes. It should be noted, however, that for a correct treatment of MOPA systems, especially with high power injected signals, the effects of gain and index saturation must be included in a self-consistent manner. One other drawback to the locked cavity mode description of a MOPA is its complexity and cumbersome mathematical calculations. The perturbed cavity modes must be found and an overlap integral of the injected beam with each cavity mode must be performed for each injection arrangement.

MOPA as a Simple Regenerative Amplifier

The theoretical analysis of a MOPA system can be greatly simplified, while retaining a surprising degree of accuracy, by treating the system as a simple regenerative amplifier. Abbas, et. al., proposed an especially simple model of a broad area MOPA system in a 1988 paper [17,58]. This model, the RGBA model mentioned earlier, assumes that the overall round trip gain, including facet losses, in a two-dimensional broad area amplifier is uniformly saturated to unity. A Gaussian input beam is then injected off-axis and propagated though multiple round trips until it leaves the edge of the gain region. The transmitted fields at the front facet from each round trip are then coherently summed to obtain the amplifier output. The assumption of uniformly saturated gain is justified by the fact that in a high gain semiconductor the injected signal is amplified to its saturated value almost immediately after injection and each reflection. In addition, since a beam injected at a small angle from the facet normal is only slightly displaced by each round trip, the beams from each round trip will mostly overlap each other, giving a nearly uniform intensity, and hence saturated gain profile in the lateral direction.

This model provides an analytical solution to the MOPA far-field and near-field profiles in terms of a sum of coherent Gaussian beams. Because of the assumption of unity gain, the model does not predict the behavior of the total amplifier output power nor does it

give realistic values of the total device gain. However the model predicts with surprising accuracy the qualitative behavior of the amplifier near-field and far-field as the angle, beamwaist and wavelength of the injected signal are varied. These predictions include the production of a narrow single-lobed far-field for certain injection conditions as well as the steering of the far-field lobe with injected wavelength. This model will be developed in more detail and compared to some original experimental data in section3.

If we retain the assumption of spatially uniform, although not necessarily saturated, gain but include the spectral characteristics of the regenerative gain, we can learn more about the amplifier behavior. The formula for the overall reflected field amplitude gain of a gain-loaded Fabry-Perot etalon is given, for example, by Siegman:

$$\frac{E_r}{E_i} = \frac{r_1 - r_2 g_{rt} e^{i\phi_{rt}}}{1 - r_1 r_2 g_{rt} e^{i\phi_{rt}}}, \tag{1}$$

where g_{rt} is the round trip field amplitude gain, ϕ_{rt} is the round trip phase delay, and r_1 and r_2 are the mirror reflection coefficients [59]. Taking the squared magnitude, we get the overall reflected intensity gain:

$$\frac{I_r}{I_i} = \frac{R_1 + R_2 G_{rt} - 2\sqrt{R_1 R_2 G_{rt}} \cos\phi_{rt}}{(1 - \sqrt{R_1 R_2 G_{rt}})^2 + 4\sin^2(\phi_{rt}/2)\sqrt{R_1 R_2 G_{rt}}}, \tag{2}$$

where $G_{rt} = g_{rt}^2$ is the round trip intensity gain and $R_1 = r_1^2$ and $R_2 = r_2^2$.

Eq.(2) is plotted in Fig.(1.1). The first thing to notice about Eq.(2) is that the magnitude of the Fabry-Perot gain ripple depends on the factor $\sqrt{R_1 R_2 G_{rt}} = r_1 r_2 g_{rt}$. Thus if we wish to limit the maximum magnitude of the gain ripple, the higher the round trip amplifier gain becomes, the smaller we must make our facet reflectivities. Or conversely, for a given allowed gain ripple, the size of the facet reflectivities of our amplifier limit the round trip gain level at which the amplifier can be operated. This shows why operating an amplifier in the nonlinear, highly saturated regime imposes less stringent requirements on the quality of the amplifier's anti-reflection coatings than does operation as a linear small-signal amplifier. In the highly saturated regime the round trip gain is clamped to a value much smaller than its unsaturated value and thus the facet reflectivity can be much larger for a given allowed gain ripple.

The other important point to notice about Eq.(2) and Fig.(1.1) is that a gain loaded Fabry-Perot cavity can act as a regenerative amplifier even when it is operated above threshold and is in steady state self oscillation. To see this consider just one of the resonant peaks in Fig.(1.1), for example, the one nearest the peak of the material gain spectrum. From Eq.(2) we see that as the round trip gain approaches its threshold value equal to the round trip losses the peak gain asymptotically approaches infinity. Of course when the laser actually begins to oscillate the peak gain is saturated to unity. However, a small external signal tuned slightly off-resonance will still receive gain when injected into the laser cavity.

In the case of a high gain semiconductor laser with one facet high-reflection coated, for example, a small, slightly off-resonance signal injected into the free running laser will

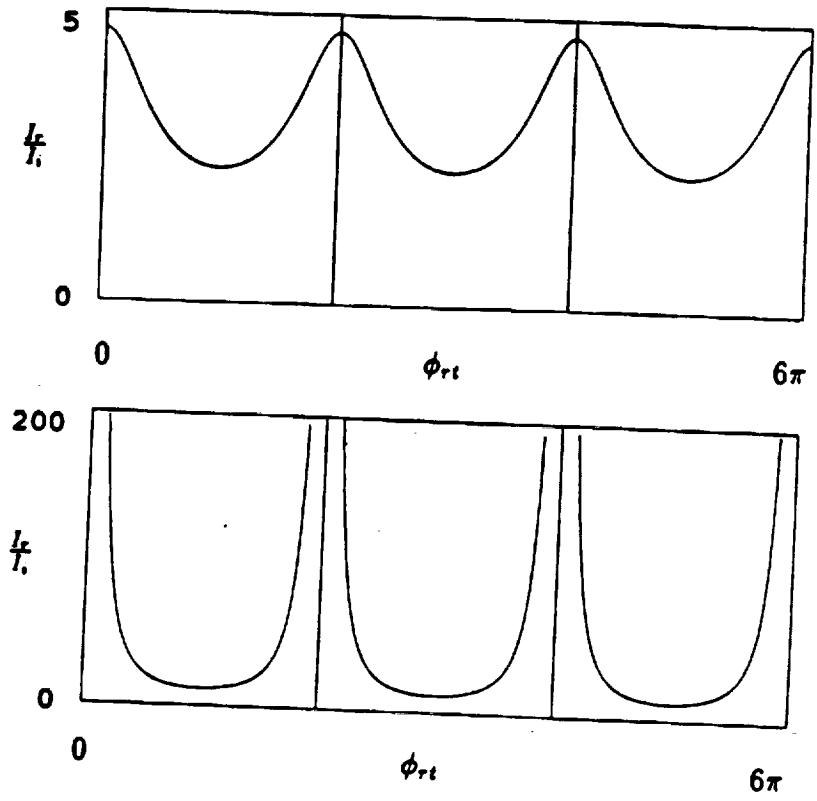

Figure 1.1: Reflective Fabry-Perot Amplifier Gain. Top: 0.2 of threshold. Bottom: 0.9 of threshold.

experience a large gain in one round trip, transmit most of its power back out the front facet and then begin a second round trip with slightly less power than when it began its first. This continues for several round trips, each pass contributing to the reflected power gain, until the signal is reduced to zero. In this way, even though the gain medium is saturated by the free running oscillation, the injected signal can see a significant amount of gain.

Now consider what happens when the injected signal is tuned increasingly close to the oscillation frequency (or the injected power is increased for a fixed off-resonance tuning). The gain seen by the injected signal increases and hence the internal fields at the injected frequency become increasingly large. At some point the fields at the injected frequency become comparable to the fields at the oscillation frequency and begin to saturate the gain seen at the oscillation frequency. Beyond this point the injected fields become sufficiently large to completely quench the free running oscillation and the device output consists entirely of amplified radiation at the injection frequency. If one calculates the full spectral width between the points on either side of resonance for which a given injected power will quench the free running oscillation, the result is exactly the locking bandwidth derived by Adler or Tang and Statz [9,13,59]. When a device is operating in this steady state condition, whether to describe it as a saturated regenerative amplifier or an injection locked oscillator becomes merely a matter of viewpoint.

REVIEW OF PREVIOUS NUMERICAL MODELING RESULTS

Due to the availability of modern high speed computers and the development of sophisticated numerical techniques, the numerical modeling of semiconductor lasers has evolved alongside the analytical theory. In fact, because of the strong interdependence of the physical properties of a semiconductor laser, numerical modeling has in many respects outpaced analytical theory. In this section the evolution of these modeling efforts will be reviewed.

Modeling of Free Running Laser Diodes

The first important self-consistent numerical model of semiconductor lasers was reported by Agrawal in 1984 [60]. This model used a beam propagation method based on fast Fourier transforms to solve the paraxial wave equation in a single stripe geometry laser diode. This useful technique will be discussed in detail in section 3. The model also solved a nonlinear carrier diffusion rate equation, including spontaneous emission and Auger recombination, along with a carrier density dependent expression for the flow of injected carriers through the active region. The model started off with an arbitrary field profile at one facet and then solved iteratively for the field and carrier density profiles, with mirror reflectivity boundary conditions at the facets, until a steady state solution was achieved. The self-consistent solution found for a set of array parameters corresponds to the sum of all the modes oscillating at that power level. Agrawal also reported a related model using the beam propagation method to analyze laser diode arrays [61]. This model only treated the near threshold regime where stimulated emission could be neglected. The resulting field profiles were interpreted as the highest gain oscillation mode that first reaches threshold.

Hadley, et. al., then published a series of papers refining this type of model. The first such paper applied the methods of Agrawal's first model to gain-guided laser diode arrays

at arbitrary power levels [62]. This analysis predicted the existence of modes of order higher than that allowed by supermode theory and hence contributed to the evidence that supermode theory was inappropriate for gain-guided arrays. The model was revised to include active region heating in a paper published in 1987 [63]. This paper also described a technique previously developed by Feit and Fleck [64] in which the beam propagation method and the Prony method are employed to calculate the propagation constants and field profiles for the eigenmodes of a structure with arbitrary gain and index profiles. The same model was applied to broad area devices as well as arrays in the following year [57]. The results of these calculations agreed quite well with the experimental observations and this model still stands as the most comprehensive analysis of gain-guided laser diodes available. In addition the eigenmodes calculated by the Prony method are strikingly similar to those recently predicted by the coupled broad area mode calculation of Verdiell [56].

Modeling of Injection Locked Laser Diodes

Hadley, et. al., also applied their highly successful modeling methods to injection locked laser diode arrays. A 1986 paper decribed the first application of the beam propagation method solved self-consistently with the carrier diffusion equation to injection locked diode arrays [20]. This model was the same as that in the previously mentioned free running analysis [62] except that the boundary condition at the array's front facet included an externally imposed field along with the facet reflection. The agreement with experimental observation was quite good, including the far-field beamsteering with injected wavelength. A similar approach was taken by Chun, et. al., in 1989 to find the optimum injection conditions for producing a single, high power, diffraction-limited output lobe [21]. It was found that a beam that covers 50% of the active region facet injected at an angle of 5° produces the maximum power in the single far-field lobe.

A simplification can be made to this type of model by simply neglecting the free running oscillations. A device operating below threshold or in the highly saturated above threshold regime can in fact be treated as a simple regenerative amplifier, as noted in the previous section. In this case, the free running oscillation can be neglected while still accurately modeling the device behavior. This simplification was made by Dente and Tilton in a recent modeling effort that also neglected spontaneous emission and Auger recombination in order to linearize the carrier diffusion rate equation [16]. The results of this model agreed very well with the recent high power experimental results in highly saturated, low facet reflectivity MOPAs [24,25,28]. A model of this type has also been developed for the present work and it will be analyzed in detail in section 3.

EXPERIMENTAL STUDY OF A FIBER COUPLED MOPA

There is little doubt that the semiconductor MOPA promises to be an important high power, high efficiency, coherent source of near infrared light. The MOPA configuration allows the exploitation of the extremely high optical gain in a semiconductor active medium without the multiple-mode, low-coherence, non-diffraction-limited behavior found in high power single element semiconductor laser diodes. On the other hand, MOPAs have the disadvantage of added size and complexity relative to single element devices.

The MOPA systems reported to date use discrete bulk optical components to establish free space coupling between the master oscillator and the amplifier. This drastically increases the size and weight of the overall system, considerations which are especially important in space based applications. In addition, because of the small size of semiconductor devices and the challenging problem of decoupling amplifier input and output, MOPA systems are alignment sensitive. Use of discrete optical components in the coupling path therefore introduces tight alignment tolerances into the MOPA arrangement.

There are a number of possible techniques for alleviating these drawbacks. A monolithically integrated MOPA may be the ultimate solution, eliminating coupling optics altogether, but this requires a significant improvement on the existing semiconductor processing technologies. Soldered optics is another possible way of preventing MOPA coupling misalignments, although this technique does not reduce the system size and weight significantly. The technique that has been explored in the present work is fiber optic master oscillator coupling. The fiber coupled MOPA (FCMOPA) employs a single mode optical fiber to transport light from the master oscillator to an epoxied miniature optics head which shapes the injection beam and decouples the reflective amplifier output.

EXPERIMENTAL ARRANGEMENT

Laser Diode Characteristics

The master oscillator used in these experiments was a 100 mW single mode laser diode manufactured by Spectra Diode Labs (model SDL-5410-G1). The diode was in the standard SOT-148 window package. This device was an index-guided, single quantum well, graded index separate confinement heterostructure (GRINSCH) laser which utilized impurity-induced disordering for longitudinal mode stabilization. Its rated temperature tuning coefficient was 0.3 nm per degree Celsius and its current tuning coefficient was 3.5 x 10^{-3} nm/mA. Its power versus current characteristic is shown in Fig.(2.1). Fig.(2.2) shows the spectrum of the master oscillator at 16° C measured on a high resolution grating spectrometer.

The power amplifier (or slave oscillator) in this arrangement was a gain-guided, single stripe BAL custom made by Spectra Diode Labs. The active region was 400 μm wide and 500 μm long and the optical waveguiding region was 1 μm high with a manufacturer specified confinement ratio of $\Gamma = 0.044$. The device was mounted active side down in the open heat sink (or C-mount) package. This package was temperature stabilized to 0.1° C by a feedback controlled Peltier cooler that was fixed on a water cooled heat sink. The device had a multiple quantum well structure with four quantum wells. The back facet

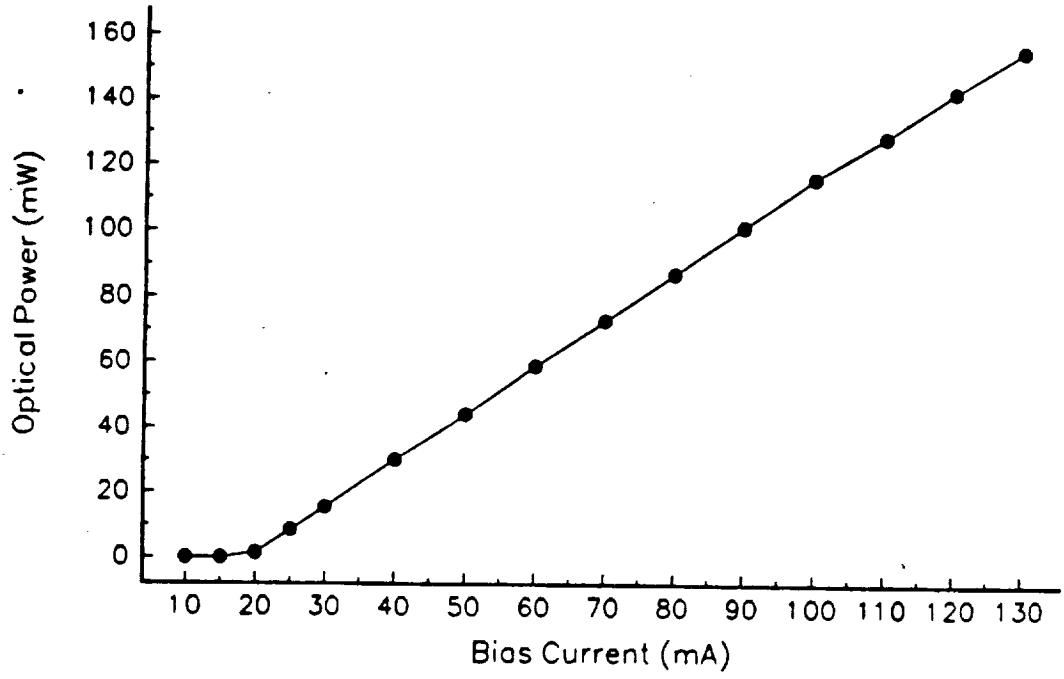

Figure 2.1: Power versus Current for MO at 18° C.

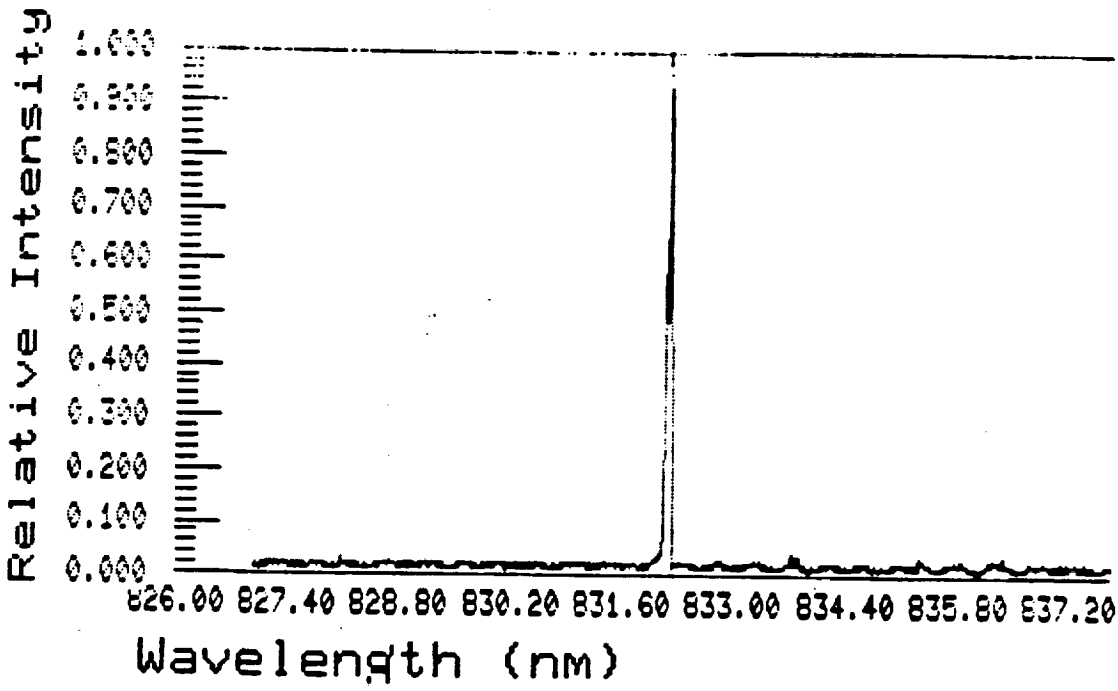

Figure 2.2: MO spectrum at 20° C.

was high reflection coated with $R_2 \approx 1$ and the front facet was antireflection coated with $R_1 \approx 0.05$. The cw bias current was provided by two Spectra Diode Labs laser diode drivers. One model SDL-800 1A driver and one model SDL-800M 2A driver were used. The measured optical power versus current characteristic for the BAL at 35° C is shown in Fig.(2.3). This shows an external quantum efficiency of 0.86 W/A. The spectrum of the BAL free running at 2.1A and 40° C was measured on a coarse grating monochromator. The result is shown in Fig.(2.4), which demonstrates a spectral full width at half maximum power of approximately 4.8 nm. Fig.(2.5) shows the BAL's free running far-field pattern, which contains two major far-field lobes.

Single Mode Fiber Coupling

Efficient coupling of master oscillator light into a single mode fiber was accomplished using a compact, stable coupling mount manufactured by Oz Optics Limited of Ontario, Canada. This arrangement included a graded index (GRIN) lens to collimate the master oscillator output which was then passed through a 30dB Faraday effect optical isolator. Another GRIN lens was epoxied to the end of the single mode fiber and was used to focus the collimated light into the fiber. Light exiting the fiber was again collimated to a 200 μm diameter spot by a third GRIN lens which was also epoxied to the fiber. This arrangement allowed 38% fiber coupling efficiency that remained stable indefinitely. The GRIN lenses used were approximately 1 mm in diameter by 5 mm in length and the coupling assembly was quite small. The size limiting component in the arrangement was the optical isolator. Future FCMOPA systems striving for compactness may benefit from the use of fiber-embedded in-line isolators such as that described by Shiraishi, et al. [65].

The inclusion of isolation in the MOPA system is important for maintaining the stability of the single mode master oscillator. Feedback of master oscillator light by reflection from optical surfaces and coupling of BAL light into the master oscillator cavity can both induce instabilities and mode-hopping in the master oscillator. These instabilities then also appear in the amplified MOPA output. For some alignment conditions feedback induced instability and mode-hopping were observed in the master oscillator even with the Faraday effect isolator in place. Fig.(2.6) shows the effect of this mode-hopping on the master oscillator spectrum. This figure is similar to Fig.(2.2) except the spectrum of the fiber-coupled master oscillator is averaged over several seconds while mode-hopping was occurring. Since unaveraged spectra showed single mode operation, the multiple peaks in the time averaged spectra must represent modes that existed at different times during the averaging period. One added advantage of a fiber coupled MOPA configuration is that the single mode fiber offers additional isolation of the BAL output from the MO cavity. This is because of the angular separation between the injected master oscillator beam and the locked BAL output which strongly reduces the amount of BAL power that is coupled back into the fiber and hence back into the MO.

Shaping the Injected Beam

As mentioned above, the master oscillator light exiting the fiber was collimated to 200 μm by a GRIN lens. This beamwidth was chosen to illuminate half of the BAL facet, as suggested by the work of Chun, et al. [21]. Immediately before the BAL facet, the circular

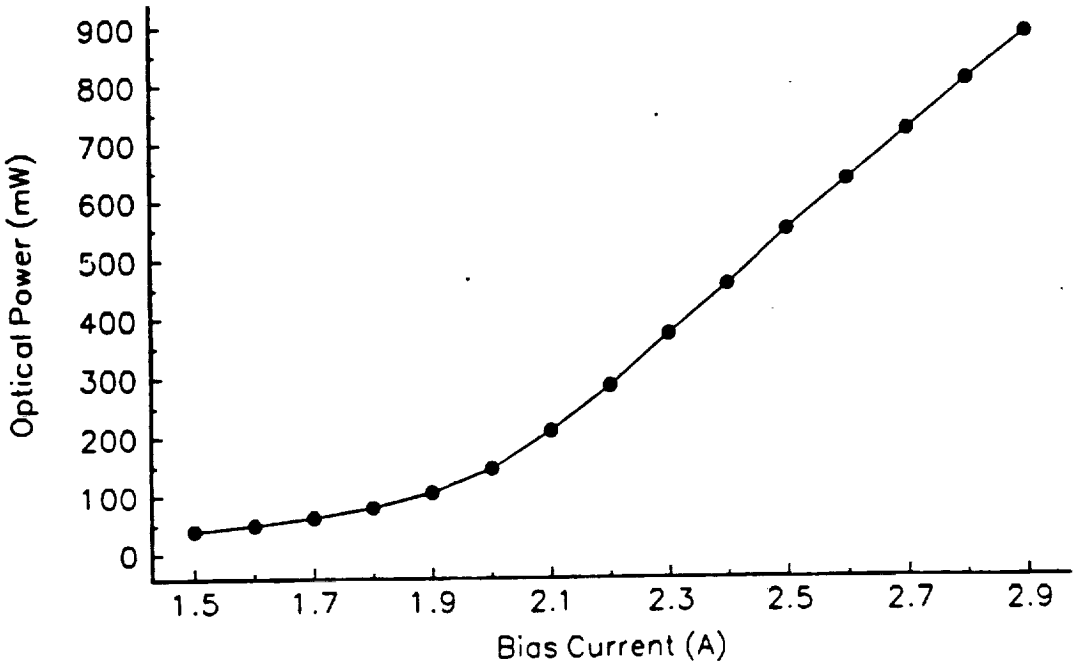

Figure 2.3: Optical Power versus Bias Current for the Free Running Broad Area Laser at 35°C.

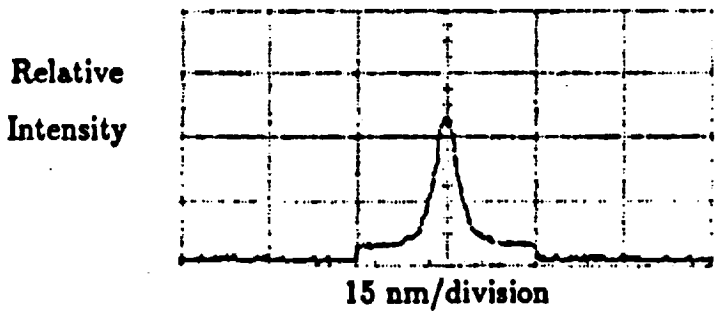

Figure 2.4: Monochromator Measurement of BAL spectrum. Spectral width is 4.6 nm.

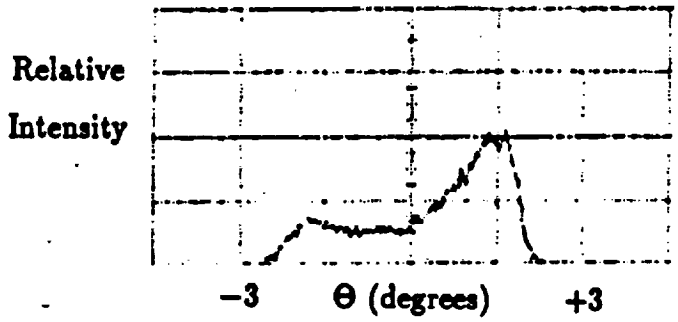

Figure 2.5: Free Running Farfield Pattern from BAL.

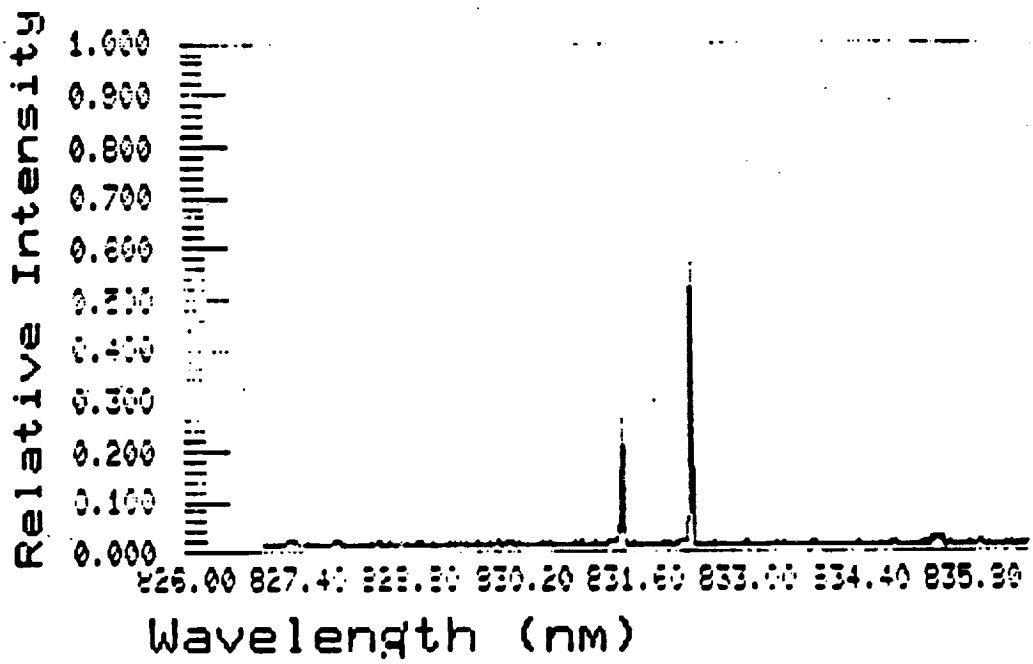

Figure 2.6: Time averaged fiber coupled master oscillator spectrum. Mode hopping is evident.

collimated injection beam was focused to a 10 μm spot in the direction perpendicular to the BAL junction plane by a miniature cylindrical lens. This lens consisted of a 2 mm diameter glass rod, 7 mm long, which was halved lengthwise and polished to form a plano-convex cylindrical lens. The same lens also served to collimate the output of the BAL in the sharply diverging transverse direction. This lens was chosen for its fairly small focal length (on the order of the rod diameter, 2 mm) and its ease of availability; however, the performance of the lens could have been improved upon. For example, the lens should ideally have been antireflection coated for the operating wavelength. In addition, a lens that produced a smaller spotsize would have provided more efficient coupling of the injected beam into the very narrow (1 μm) facet of the BAL. Finally, the small lens failed to capture much of the quickly diverging BAL output resulting in a significant reduction in useful MOPA output power.

Decoupling the MOPA Output

One of the challenging engineering problems in building a reflective MOPA system is decoupling the MOPA output from the injected input beam. Most previously reported systems used the small angular separation between the two beams to separate them via a sharp pick-off mirror. This technique requires precise alignment of the mirror and injection angle and does not lend itself well to miniature, alignment-insensitive applications. The current experiment employs a polarization decoupling scheme which takes advantage of the nearly linear polarization state of the laser diode outputs. An outline of the complete experimental setup is shown in Fig.(2.7).

The setup includes a polarizing beam splitter and a birefringent element in addition to the beam shaping optics discussed in the last section. Ideally, the birefringent element would have been a Faraday effect polarization rotator. In this system the fiber coupled master oscillator would be aligned with its polarization 45° from the BAL junction plane. The beamsplitter would be arranged to completely transmit master oscillator beam. The Faraday rotator would then rotate the polarization of the beam by 45° into the junction plane of the BAL. The linearly polarized BAL output would then re-enter the Faraday rotator and its polarization would be rotated another 45° so that it was orthoganal to the input. The polarizing beamspliter would then deflect the output and achieve the desired decoupling. This arrangement would require a preferably miniature Faraday rotator operating at the system wavelength that would tolerate the propagation of two spatially separated beams at angles several degrees removed from the axis of the birefringent crystal. Unfortunately, this technology is not yet available.

An adequate alternative was used in this experiment to demonstrate the operation of the FCMOPA system. The above arrangement was used except that a $\frac{\lambda}{4}$ waveplate was substituted for the Faraday rotator. The result was that the linearly polarized beam leaving the fiber was converted to circular polarization by the $\frac{\lambda}{4}$ waveplate. Only half of the resulting circularly polarized beam was then efficiently coupled into the BAL active region. In addition, the BAL output was also converted to circular polarization and half of its output power was lost due to transmission at the polarizing beam splitter. The total effect of this substitution was the requirement of twice as much master oscillator power for a given injection level and the loss of 3 dB of MOPA output power.

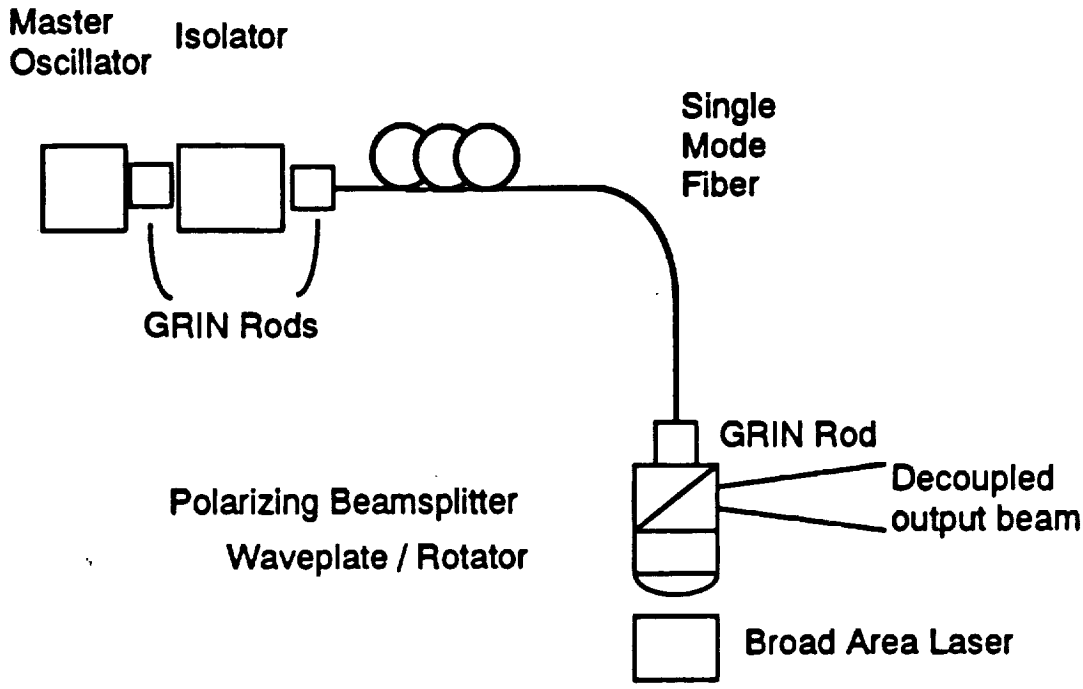

Figure 2.7: Experimental Arrangement of Fiber Coupled MOPA.

Miniaturization and Alignment Insensitivity

All of the beam shaping and output decoupling components used in this experiment were miniature optics. The largest component was the polarizing beamsplitter which was a cube 7 mm on a side. The beamsplitter and the $\frac{\lambda}{4}$ waveplate were permanently epoxied together. The fiber pigtailed collimating GRIN lens and the focusing cylindrical lens were arranged in direct contact with either side of the beamsplitter-waveplate assembly and could also have been epoxied together. As a result the entire beam shaping and output decoupling assembly formed a single, rigid, miniature, alignment insensitive optics head attached to the end of the single mode fiber. The only remaining free space optical path still subject to misalignment was the space between the final focusing lens and the BAL facet. This gap could also be closed by manufacturing a cylindrical lens monolithically integrated with an optical blank of different refractive index. This component could then be epoxied between the BAL and the birefringent element hence eliminating all movable alignment joints.

Diagnostics Arrangement

Both the far-field emission pattern and the emission spectrum of the FCMOPA system were monitored. The spectrum was monitored at the beamsplitter output using the same grating monochromater used for Fig.(2.4). The far-field emission pattern was monitored using a linear array charge coupled device (CCD) camera. The CCD array consisted of a single row of adjacent 25 μm wide CCD elements which were read out linearly and displayed on a digital oscilloscope. A similar array was employed as the detector component of the monochromator used in the spectrum measurements. The far-field monitoring CCD camera was placed above and in front of the BAL facet so that the far-field could be detected from the portion of the BAL emission that was not captured by the cylindrical lens. Only the profile of the far-field pattern along the axis parallel to the BAL junction plane is of interest in the injection locking study.

EXPERIMENTAL RESULTS

Observation of Injection Locking

Successful injection locking of the FCMOPA configuration was observed in this experiment. After the spectra of the BAL and the master oscillator were temperature tuned into proximity as monitored on the monochromator, the alignment of the injection beam with the BAL facet was adjusted until the far-field pattern became predominantly single lobed. At this point injection locking was achieved.

Fig.(2.8) shows a typical observed injection locked far-field pictured below the corresponding free running far-field pattern. In this particular case it can be seen that injection locking was achieved for injection angles significantly smaller than the 5° suggested by Chun, et al. [21]. For this measurement the BAL was biased at 2.1 A corresponding to a free running power of 210 mW and was operating at 40° C. Based on the measurement of the area under the various parts of the curve in Fig.(2.8) it was calculated that approximately 65% of the total output power was contained in the single main lobe. The angular half width of the single lobe is 0.18° which is 1.5 times the diffraction limit. The diffraction

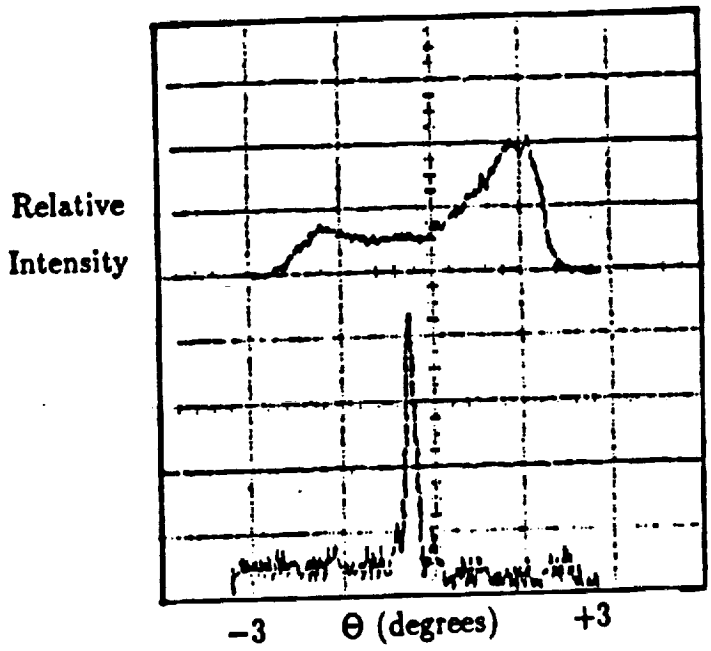

Figure 2.8: Farfield Patterns. Top: free running. Bottom: injection locked.

limit is defined as the angle of the first null in the diffraction pattern of a uniformly illuminated slit of width D equal to the width of the BAL facet. Numerically, the diffraction limit is approximately $\Theta_{null} = \frac{\lambda}{D} = 0.12°$.

The actual useful power coupled out through the polarizing beamsplitter of the FCMOPA was typically only on the order of a few tens of mW. This is much less than the 65% of the total free running power estimated from Fig.(2.8). This loss of power results from two causes. The first is the losses associated with the cylindrical lens, which were discussed above. The lens fails to capture a large portion of the BAL emission. The second is the 3 dB loss associated with the use of the $\frac{\lambda}{4}$ waveplate instead of a Faraday rotator. Efficient output decoupling is the major area in which a practical high power FCMOPA system will require significant engineering development.

A typical FCMOPA spectral measurement using the grating monochromator is shown in Fig.(2.9). The top trace in this figure is the same as that shown in Fig.(2.4) and shows the free running BAL spectrum. The lower trace shows the significantly narrowed injection locked spectrum of the FCMOPA. It should be noted that the CCD camera was saturated at the peak of this particular trace so that the spectral width of the injection locked BAL is not evident. In addition, the resolution of the monochromator is not sufficient to verify single mode operation in the injection locked trace or to resolve individual modes in the free running case. However, it is clear that injection locking significantly reduces the source linewidth and it is reasonable to assume, based on similar experiments with free space coupled MOPAs, that Fig.(2.9) represents single mode operation of the FCMOPA.

Observation of Beamsteering Effects

Injection locking was achieved with spectra and far-field patterns similar to those described above for a range of injection angles up to 5°. The locked far-field lobe could be optimized for a particular injection angle by tuning the current or temperature of either the master oscillator or the BAL or both. The optimized locked lobe would be emitted near the angle opposite the injection angle. Tuning the current or temperature of either or both of the laser diodes also resulted in the steering of the locked lobe across the far-field. As the master oscillator current, for example, was increased from zero an injection locked far-field lobe would appear in the emitted far-field pattern. As the current was increased further the locked lobe would steer across the far-field through an envelope with a peak near the angle opposite the injection angle. As the lobe passed the peak and disappeared out the edge of the envelope, a new locked lobe would appear at the other edge. One complete sweep of the locked lobe was observed as the master oscillator current was tuned over a range of 20–25 mA. This current change corresponds to a wavelength change of 0.7–0.9 Å. Tuning of the BAL bias or the temperature of either device lead to similar behavior of the far-field lobe. This behavior is consistent with the simple RGBA model to be discussed in the next section.

Conclusions of Experimental Study

The successful demonstration of injection locking and amplification in a fiber coupled MOPA system was achieved. A polarization based output decoupling scheme was described and demonstrated. The spectrum and far-field pattern of the FCMOPA system were

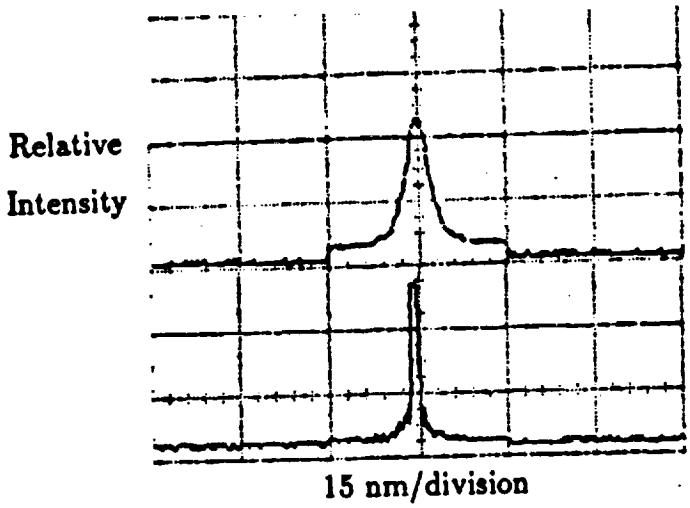

Figure 2.9: BAL Spectra. Top: free running. Bottom:injection locked.

measured and found to be consistent with similar studies of free space coupled MOPAs. The behavior of the FCMOPA far-field during current and temperature tuning of the laser diodes was described and also found to be consistent with previously reported observations.

While it was demonstrated that it is feasible to build a fiber coupled MOPA system, it is also clear that a great deal of engineering development would be required to realize a practical FCMOPA. The output decoupling subsystem is the portion of the FCMOPA that would require the most development. An efficient polarization based decoupling scheme will depend on the development of advanced Faraday rotators or optical circulators. Practical decoupling and beamshaping optics will also benefit from the development of advanced optical materials processing and machining for the manufacture of improved cylindrical lenses and optical blanks such as those discussed above. Whether a practical FCMOPA is developed may depend on whether the above technologies or the monolithically integrated semiconductor MOPA are the first to mature.

MOPA SIMULATION STUDIES

The understanding of semiconductor lasers and MOPA systems has been greatly augmented by extensive numerical modeling and simulation. Section 1 briefly discussed a number of important numerical modeling efforts that have been reported previously. In the current work two separate models are developed. The first is the numerical calculation of the results of the very simple analytical RGBA model first proposed by Abbas, et al [17]. The second is a simplification of the fast Fourier transform (FFT) beam propagation method (BPM) model of the type used by Hadley, et al. [20], Chun, et al. [21], and Dente and Tilton [16]. In addition a new version of the FFT BPM model will be developed that includes the effects of amplified spontaneous emission (ASE).

THE RGBA MODEL

Description of the RGBA Model

The RGBA model describes the behavior of a reflective Fabry-Perot regenerative semiconductor amplifier entirely in terms of two-dimensional Gaussian beams. The third dimension, transverse to the amplifier junction plane, is neglected since the amplifier acts as a single mode planar waveguide in that dimension and the effective index approximation can be applied [66,67]. Hence, the model provides an analytical expression for the amplifier fields. However, this expression is a summation over several Gaussian beam fields and is best evaluated numerically.

In this model the injected beam is assumed to be a Gaussian beam that is focused to a beamwaist at the amplifier facet. The beam undergoes Snell's law refraction at the facet and then propagates through the device, reflects off the perfectly reflecting back facet and then propagates back through the device to the front facet. All inhomogeneities in the gain and refractive index inside the amplifier cavity are neglected so effects such as spatial hole burning and thermal lensing are not modeled. The small signal gain in the amplifier is assumed to be sufficiently large that the injected beam is immediately amplified inside the front facet to the point where the device gain is uniformly saturated. When the injected beam returns to the front facet the majority of its power is transmitted and contributes to the amplifier emission. The small reflected portion is again assumed to be immediately amplified to the level of uniform saturation. This beam thus continues to propagate through several passes until it walks off into the absorbing unpumped regions on the edges of the amplifier. The output of the amplifier is taken to be the coherent sum of the equal amplitude contributions of each internal round trip transmitted at the front facet. Fig.(3.1), taken directly from reference [17], is a sketch of the this situation.

Mathematical Development of RGBA Model Calculation

The development given below is essentially the same as that given by Abbas, et al. in their original presentation [17]. In order to calculate the near-field and far-field profiles of the amplifier, the contributions from transmission at each round trip of the injected beam are treated as separate coherent Gaussian beams each with its own effective origin and coordinate system. Actually, due to the difference in the variation of the real and imaginary parts of the exponent in the standard Gaussian beam expression (see Eq.(11))

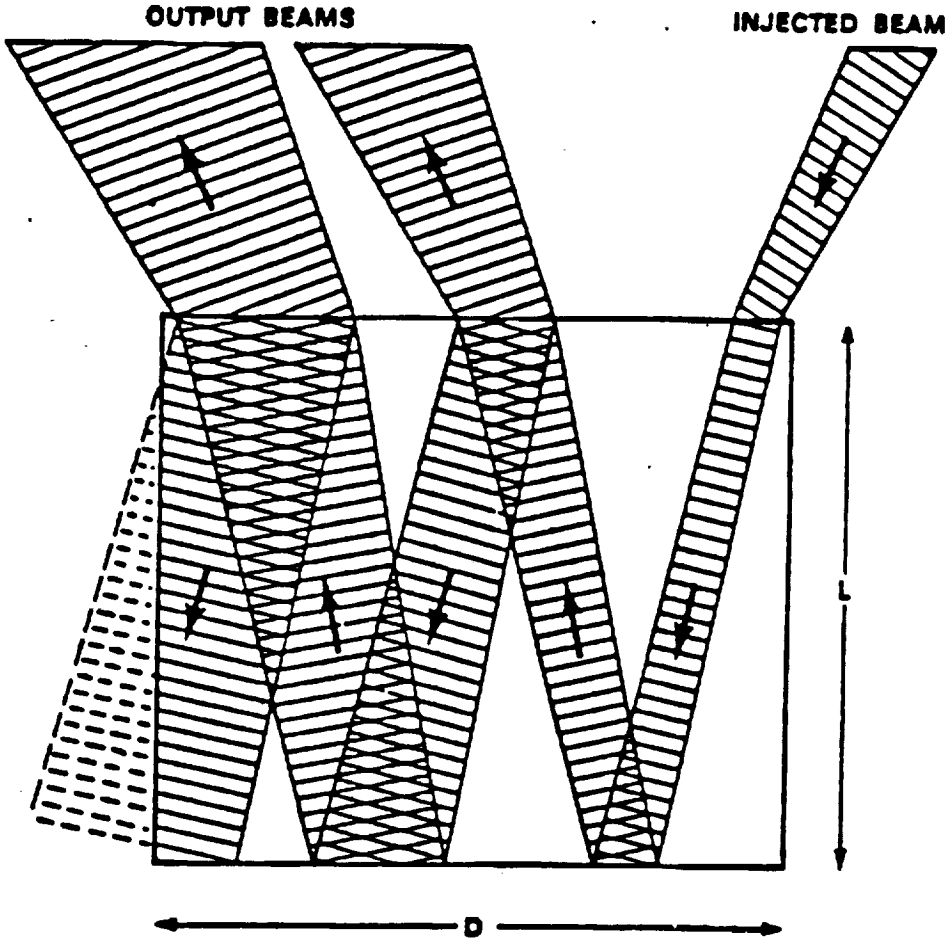

Figure 3.1: Sketch showing gaussian beams in the RGBA model (From reference [17]).

with distance, each transmitted Gaussian beam has two effective origins: one for the calculation of phase and the other for the calculation of amplitude. The effective origin of the ith Gaussian beam for the amplitude calculation is defined as (x_{ai}, z_{ai}). The effective phase origin is (x_{pi}, z_{pi}). Fig.(3.2), also taken directly from reference [17], shows the path taken in the first round trip of the injected beam and defines the other important parameters in the following development. The coordinate system is defined with z along the length of the amplifier, x along its width, and the origin located at the left edge of the front facet.

We let Θ_I be the internal angle of propagation relative to the z coordinate. Its value is determined by Snell's law as:

$$\sin\Theta_I = \frac{1}{n}\sin\Theta_0. \tag{3}$$

The actual distance traveled by a beam at angle Θ_I in one round trip is L' where

$$L' = \frac{2L}{\cos\Theta_I} \tag{4}$$

With these definitions the effective phase and amplitude origins for the ith beam can easily be found to be as follows:

$$\begin{aligned} x_{ai} &= x_{in} + i\cdot\left(\frac{L'}{n}\sin\Theta_0 - 2L\tan\Theta_I\right) \\ &= x_{in} \end{aligned} \tag{5}$$

$$z_{ai} = -i\cdot\frac{L'}{n}\cos\Theta_0 \tag{6}$$

$$x_{pi} = x_{in} + i\cdot(L'n\sin\Theta_0 - 2L\tan\Theta_I) \tag{7}$$

$$z_{pi} = -i\cdot L'n\cos\Theta_0 \tag{8}$$

The effective coordinates for any point (x, z) in the coordinate system aligned with the ith beam are defined as $(\hat{x}_{ai}, \hat{z}_{ai})$ and $(\hat{x}_{pi}, \hat{z}_{pi})$ for the amplitude and phase respectively. These coordinates can be calculated from the above effective origins using the following coordinate transformations:

$$\begin{bmatrix}\hat{x}_{ai}\\ \hat{z}_{ai}\end{bmatrix} = \begin{bmatrix}\cos\Theta_0 & \sin\Theta_0\\ -\sin\Theta_0 & \cos\Theta_0\end{bmatrix}\cdot\begin{bmatrix}x - x_{ai}\\ z - z_{ai}\end{bmatrix} \tag{9}$$

$$\begin{bmatrix}\hat{x}_{pi}\\ \hat{z}_{pi}\end{bmatrix} = \begin{bmatrix}\cos\Theta - o & \sin\Theta_0\\ -\sin\Theta_0 & \cos\Theta_0\end{bmatrix}\cdot\begin{bmatrix}x - x_{pi}\\ z - z_{pi}\end{bmatrix} \tag{10}$$

The field due to the ith Gaussian beam can now be calculated for any point (x, z) where $z > 0$, that is outside of the amplifier. The field, $E_i(x, z)$ is the standard Gaussian beam expression:

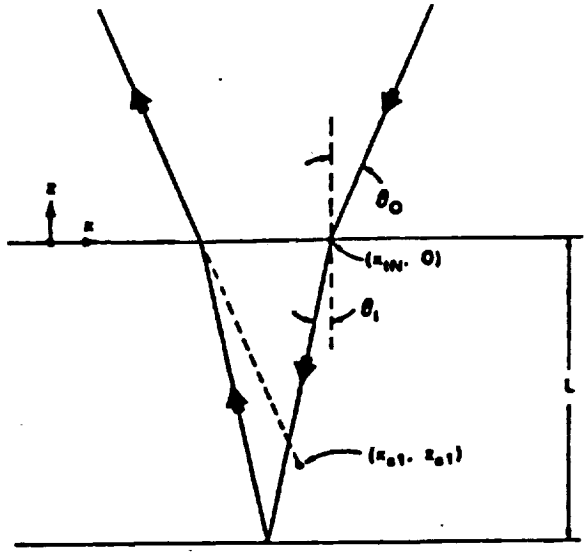

Figure 3.2: Detailed Sketch of First Pass in RGBA model (From reference [17]).

$$E_i(x,z) = E_0\sqrt{\frac{w_0}{w}} \cdot \exp\left\{-j(k_0\hat{z}_{pi} - \eta) - (\hat{x}_{ai})^2\left(\frac{1}{w^2} + \frac{jk_0}{2R}\right)\right\} \tag{11}$$

where the Gaussian beam parameters are as follows:

$$w^2 = w_0^2\left[1 + \left(\frac{\lambda\hat{z}_{ai}}{\pi w^2}\right)^2\right] \tag{12}$$

$$\eta = \frac{1}{2}\tan^{-1}\left(\frac{\lambda\hat{z}_{ai}}{\pi w_0^2}\right) \tag{13}$$

$$R = \hat{z}_{ai}\left[1 + \left(\frac{\pi w_0^2}{\lambda\hat{z}_{ai}}\right)^2\right] \tag{14}$$

where w_0 is the input Gaussian beam radius, λ is the injected beam wavelength in free space, and k_0 is the free space wave number.

The total electric field, $E_T(x,z)$ is simply the sum of all the E_i contributions

$$E_T(x,z) = \sum_{i=0}^{S} E_i(x,z) \tag{15}$$

where S is the number of round trips before the internal beam leaves the side of the amplifier cavity calculated as:

$$S = \left\lfloor \frac{D - \frac{2w_0}{\cos\Theta_0}}{2L\tan\Theta_I} \right\rfloor \tag{16}$$

The near-field at the amplifier front facet can now be easily calculated as

$$|E_T(x,0)|^2 \tag{17}$$

and the far-field profile as a function of far-field angle Θ is

$$|E_T(r\sin\Theta, r\cos\Theta)|^2 \tag{18}$$

for some large distance r.

This model was implemented in a C++ computer program and executed on an Intel 80486 based personal computer. Some typical results predicted by the model will be presented in the next section.

Predicted Results of the RGBA Model

Fig.(3.3) shows the far-field pattern predicted by the RGBA model for a wide injection beam (200 μm) injected at 5° from the facet normal. The point resolution of the model for this and all the other RGBA model figures is 1 μm. The structure of the main lobe and the nearby side lobes resembles the experimental far-field in Fig.(2.8). However, it should be noted that since the RGBA model does not consider any of the spontaneous or free running emission of the BAL, most of the far-field structure away from the locked lobe in the experimental figure does not appear in the RGBA predicted far-field pattern. Fig.(3.3) also shows the predicted near-field distribution for the same injection case.

For comparison, Fig.(3.4) shows the predicted near-field and far-field distributions obtained for a narrow injected beam (5 μm). The far-field here has a multiple-lobed, non-diffraction-limited pattern. Note that the near-field profile for the single lobed case is more nearly uniform than the near-field profile in the multiple lobed case. This is reasonable since a uniform near-field more closely resembles the uniformly illuminated aperture for which the diffraction limit is defined. Fig.(3.5) further illuminates the influence of injected spot size on the RGBA predicted far-field pattern. This figure shows the main far-field lobe for three different spotsizes with all other injection parameters fixed and illustrates that the optimum configuration has the largest injected spot (covering half of the amplifier facet) as was also predicted by the more sophisticated, self-consistent model of Chun, et al. [21]

Fig.(3.6) demonstrates another important strength of the simple RGBA model, which is its ability to predict the beamsteering effects in a semiconductor MOPA system. The figure shows a succession of far-field patterns predicted when only the injected wavelength was varied over a few Angstroms. The main far-field lobe steers through an envelope centered near the angle opposite the injection angle and after it disappears from one edge of the envelope a new lobe appears at the other edge. This behavior is identical to that observed in the experiments and described in section 2. The wavelengths in this figure are given in micrometers beside each main far-field lobe. The intensity scale on the vertical axis is arbitrary as it is in all the RGBA far-field figures.

THE FFT BPM MODEL

Description of the FFT BPM Model

The RGBA model completely neglects the influence of the charge carriers in the semiconductor MOPA active layer on the optical fields. This model also simplifies the spatial variation of the optical fields to the propagation of fundamental mode Gaussian beams. In reality, the optical fields in the MOPA depend strongly on the concentration of charge carriers and, conversely, the carrier concentrations depend strongly on the optical fields. As a result the optical fields possess detailed lateral and longitudinal spatial variation. The FFT BPM model takes a more realistic modeling approach by solving self-consistently for the optical fields and the carrier concentration in the MOPA system amplifier cavity.

The FFT BPM model uses an FFT based spectral beam propagation method to solve the paraxial wave equation for the optical fields on a rectangular mesh of points in the amplifier. A simplified carrier diffusion rate equation is solved for the carrier concentrations on the

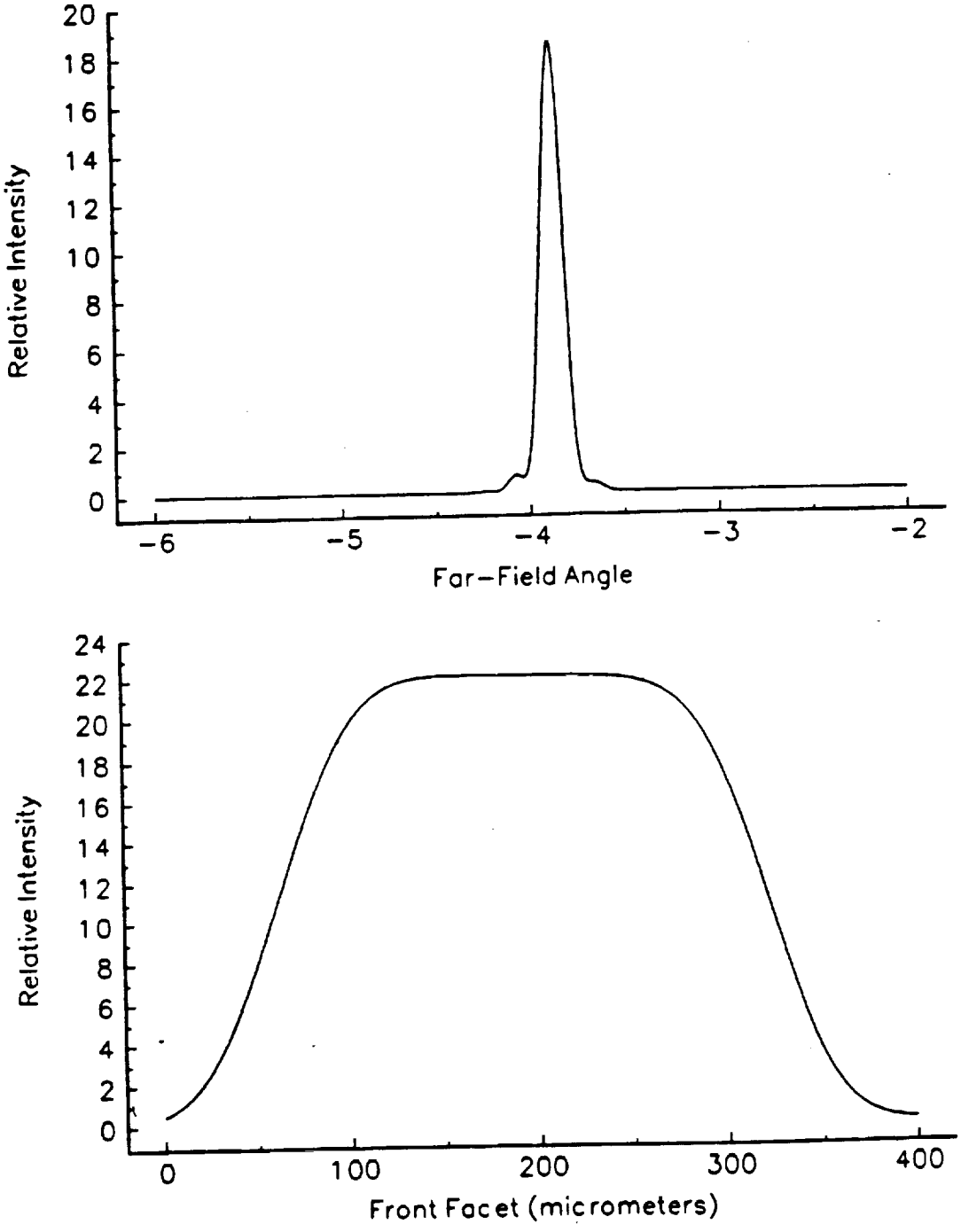

Figure 3.3: RGBA model far-field (top) and near-field (bottom) for wide injected beam.

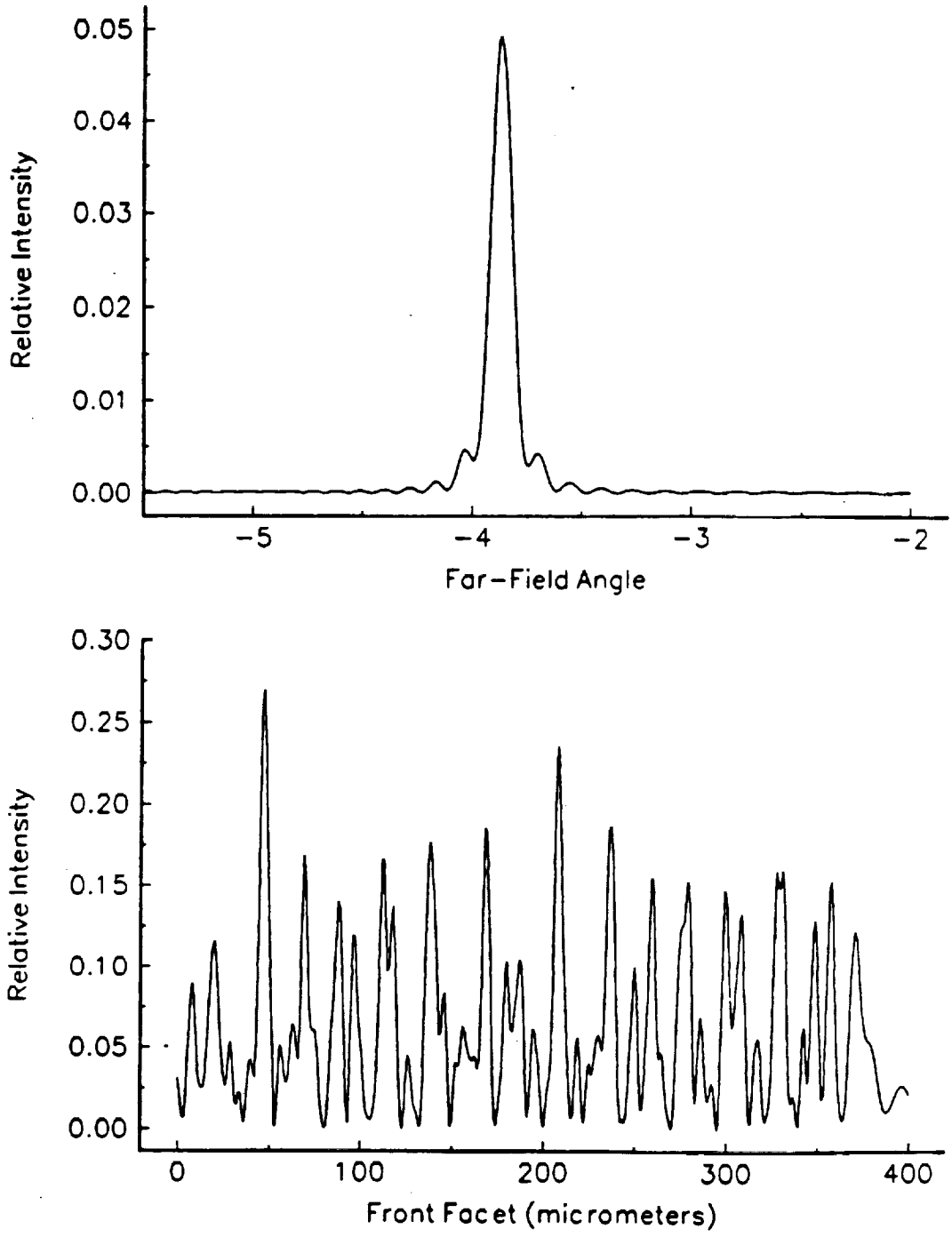

Figure 3.4: RGBA model far-field (top) and near-field (bottom) for narrow injected beam.

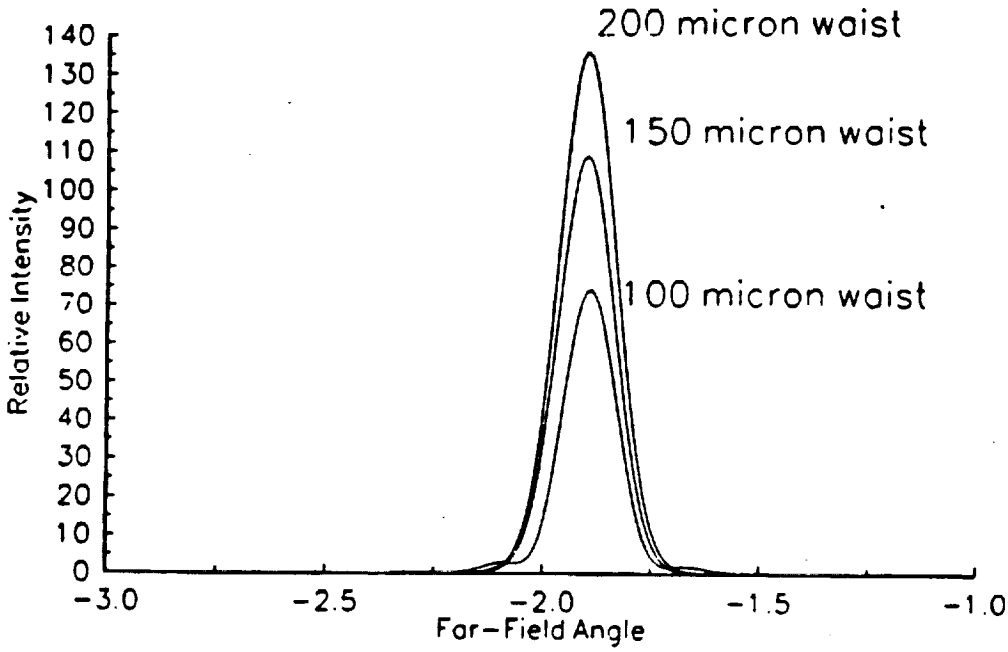

Figure 3.5: RGBA model far-fields for different injected spot sizes.

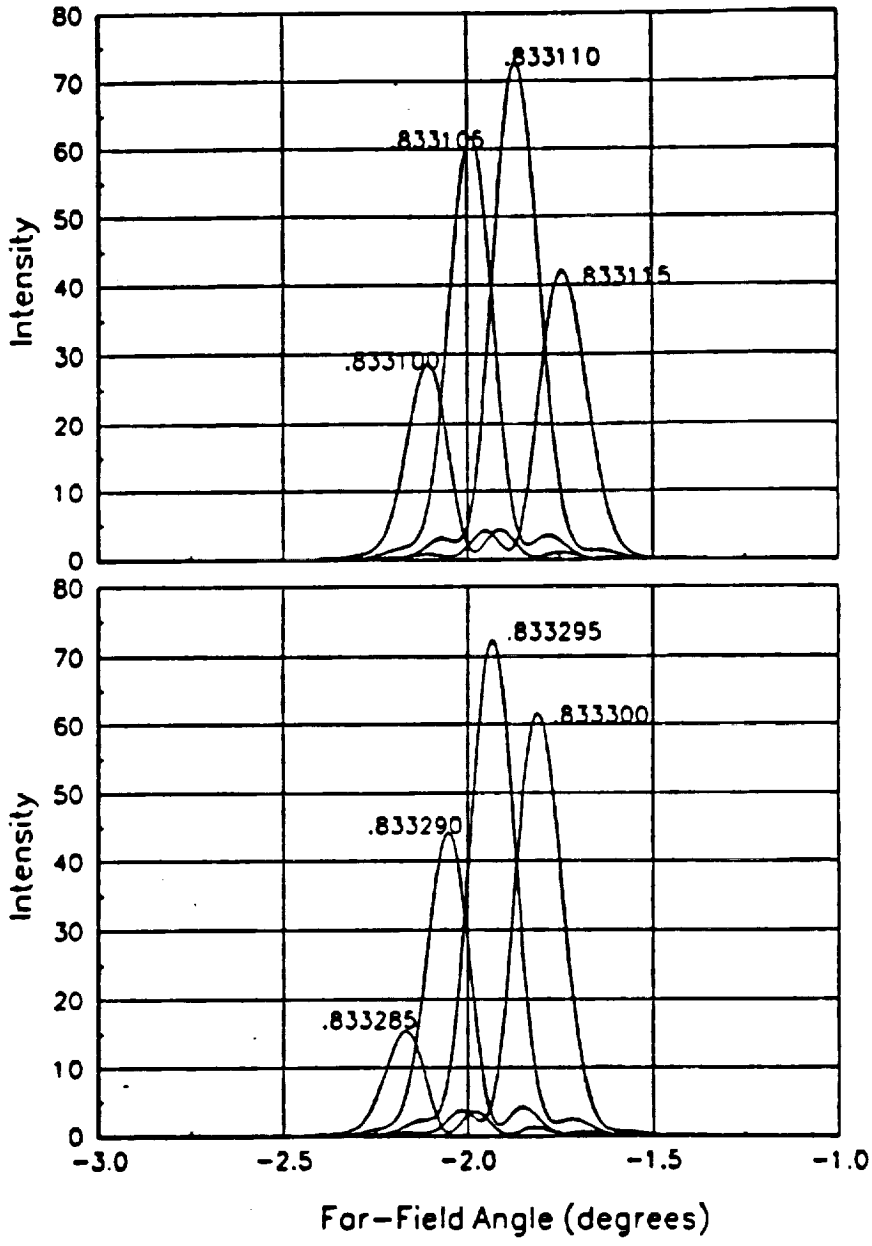

Figure 3.6: RGBA model prediction of far-field beam steering with wavelength.

same grid. The two solutions are coupled via stimulated emission, optical gain, and carrier induced variations of the refractive index. The optical gain due to stimulated emission over one mesh spacing is treated as a thin sheet of finite gain concentrated at the corresponding row of grid points. The two halves of the problem are solved iteratively until all the fields converge to a steady state solution.

The current implementation of the FFT BPM model is similar to previously reported studies ([20,21,16]) with some simplifications. For simplicity, temperature variation across the amplifier junction is neglected as is the variation in injected current density due to spatial variation of the carrier concentration dependent junction potential. Longitudinal diffusion and nonlinear recombination mechanisms have been left out of the carrier diffusion rate equation to facilitate computation. In addition, the amplifier is treated as a strictly double pass reflective traveling wave amplifier with negligible front facet reflectivity. This latter simplification is appropriate for modeling recently reported experiments with high power anti-reflection coated semiconductor amplifiers and the simulation results will be compared to those experiments rather than the FCMOPA experiments reported in section 2. The neglect of amplifier front facet reflection is further justified by observations made in the Dente and Tilton FFT BPM simulation study in which small front facet reflectivities were found to have little effect on the field profiles predicted by the model [16].

MATHEMATICAL TREATMENT OF THE FFT BPM MODEL

Solving for the Optical Fields

Spectral beam propagation methods for solving the paraxial wave equation have been known for some time. Their use has increased since the development of computationally efficient numerical discrete Fourier transform algorithms and the increased availability of high speed computer facilities. The mathematical treatment of the spectral BPM can be found in a variety of publications (see, for example, [58,59,68]) each with different approaches and with different levels of generality. The following treatment is specific to optical geometries in which the effective index approximation can be applied and it follows the same approach as that found in reference [16].

The development begins with Maxwell's equations in the following form:

$$\nabla \times \mathcal{E} = -\mu_0 \frac{\partial \mathcal{H}}{\partial t} \tag{19}$$

$$\nabla \times \mathcal{H} = \frac{\partial \mathcal{D}}{\partial t} \tag{20}$$

$$\nabla \cdot \mathcal{E} = 0 \tag{21a}$$

$$\nabla \cdot \mathcal{H} = 0 \tag{21b}$$

where $\mathcal{E}$ and $\mathcal{H}$ are the electric and magnetic fields and $\mathcal{D}$ is the electric displacement vector defined as

$$\begin{aligned}\mathcal{D} &= \epsilon\mathcal{E} + \mathbf{P}_j \\ &= \epsilon[1 + \chi_c]\mathcal{E},\end{aligned} \tag{22}$$

where $\epsilon = \epsilon_0 n^2$ is the background permittivity of the host medium, $\mathbf{P}_c = \epsilon\chi_c\mathcal{E}$ is the complex polarization induced by the carriers or active atoms, and χ_c is the associated complex susceptibility. Eq.(19), Eq.(20), Eq.(21), and Eq.(22) can be combined in the usual way to arrive at the inhomogeneous wave equation.

$$\nabla^2\mathcal{E} - \frac{n^2}{c^2}\frac{\partial^2\mathcal{E}}{\partial t^2} = \mu_0\frac{\partial^2\mathbf{P}_c}{\partial t^2} \tag{23}$$

We next assume that the electric field is polarized primarily in the lateral or x direction. It should be noted, however, that in the experiments described above the circularly polarized injected field also had a significant component in the transverse or y direction which is not included in this model. Time harmonic variation and propagation in the z or longitudinal direction are also assumed such that $\mathcal{E}$ and $\mathbf{P}_c$ have the following forms:

$$\mathcal{E} = \hat{E}(x, y; z)e^{j(kz-\omega t)}\hat{\mathbf{x}} \tag{24}$$

$$\mathbf{P} = \hat{P}_c(x, y; z)e^{j(kz-\omega t)}\hat{\mathbf{x}} \tag{25}$$

where $\hat{E}(x, y; z)$ is assumed to have only slow variation in z, $\hat{\mathbf{x}}$ is a unit vector in the x direction and $k = \frac{n\omega}{c}$ is the wave vector in the host medium. It should be noted that in assuming the e^{jkz} variation of the fields we are neglecting the fact that the wave may in fact be traveling slightly off-axis, as is usually the case in the reflective semiconductor traveling wave amplifiers of interest. In this situation k actually obeys a Pythagorean relation with the two separate directional wave numbers k_x and k_z:

$$k^2 = k_x^2 + k_z^2 \tag{26}$$

However, if this approximation is not made the result is an additional phase factor in the final expression for the propagated field that is proportional to the square of the sine of the off-axis angle. Since the internal propagation angles in the cases of interest are small and the paraxial approximation is appropriate, this phase factor can be safely neglected.

Next, we split the Laplacian operator in Eq.(23) into transverse and longitudinal components and expand the operation of the longitudinal component on $\mathcal{E}$.

$$\nabla^2 = \nabla_t^2 + \frac{\partial^2}{\partial z^2} \tag{27}$$

$$\frac{\partial^2\mathcal{E}}{\partial z^2} = \frac{\partial^2\hat{E}}{\partial z^2} + 2jk\frac{\partial\hat{E}}{\partial z} - k^2\hat{E} \tag{28}$$

Because we have assumed that $\hat{E}$ varies only slowly in z, we can ignore the first term in Eq.(28). The result of all of the above assumptions and simplifications is the scalar paraxial wave equation for $\hat{E}$.

$$\left[\frac{1}{2jk}\nabla_t^2 + \frac{\partial}{\partial z}\right]\hat{E} = \frac{jk}{2}\chi_c\hat{E} \tag{29}$$

Finally we apply the standard effective index approximation [66,67]. We divide the transverse or y axis into regions in which the background refractive index of the host medium is constant and then assume that the solution to Eq.(29) takes the product form.

$$\hat{E}(x,y;z) = Y(y)E(x;z) \tag{30}$$

Applying separation of variables yields a new paraxial wave equation for $E(x;z)$.

$$\left[\frac{1}{2jk}\frac{\partial^2}{\partial x^2} + \frac{\partial}{\partial z}\right]E = gE \tag{31}$$

where

$$g = \Gamma\left(-k\frac{\chi_c''}{2} + jk\frac{\chi_c'}{2}\right) - a \tag{32}$$

is the total complex amplitude gain coefficient, Γ is the photon confinement ratio, a is the non-saturable cladding loss coefficient and χ_c' and χ_c'' are the real and imaginary parts, respectively, of the complex carrier-induced susceptibility. All of the physical parameters relevant to this simulation are summarized in Table(2).

To allow numerical computation we must discretize the x axis. We assume that the domain of the problem is artificially embedded in a periodic domain of width a_x which is larger than the width of the actual active region. We then define x_m as the m^{th} of $\mathcal{N}_x$ points such that

$$x_m = m\frac{a_x}{\mathcal{N}_x} \quad m = 0,1,\ldots,\mathcal{N}_x - 1 \tag{33}$$

The electric field on this set of discrete points for some value of z can then be decomposed into a set of Fourier components $\phi_i(z)$.

$$E(x_m,z) = \sum_{i=0}^{\mathcal{N}_x-1}\phi_i(z)e^{j2\pi x_m\frac{i}{a_x}} \tag{34}$$

Substituting Eq.(34) into Eq.(31) yields

$$\frac{\partial}{\partial z}\sum_{i=0}^{\mathcal{N}_x-1}\phi_i(z)e^{j2\pi x_m\frac{i}{a_x}} = \left(g - \frac{1}{2jk}\frac{\partial^2}{\partial x^2}\right)\sum_{i=0}^{\mathcal{N}_x-1}\phi_i(z)e^{j2\pi x_m\frac{i}{a_x}} \tag{35}$$

Eq.(35) must be satisfied for each value of i. Thus, after noting that

$$\frac{\partial^2}{\partial x^2}e^{j2\pi x_m\frac{i}{a_x}} = -4\pi\frac{i^2}{a_x^2}e^{j2\pi x_m\frac{i}{a_x}} \tag{36}$$

we see that

$$\frac{\partial}{\partial z}\phi_i(z) = (g - \frac{j}{2k}4\pi^2\frac{i^2}{a_x^2})\phi_i(z)$$
$$= (g - j\pi\frac{\lambda_i^2}{a_x^2})\phi_i(z). \tag{37}$$

Rearranging and integrating from z to $z + \Delta z$ as

$$\int_z^{z+\Delta z} \frac{\partial\phi_i(z)}{\phi_i(z)} = \int_z^{z+\Delta z} \left(g - j\pi\frac{\lambda i^2}{a_x^2}\right)\partial z \tag{38}$$

yields

$$\ln\left(\frac{\phi_i(z+\Delta z)}{\phi_i(z)}\right) = \left(g - j\pi\frac{\lambda i^2}{a_x^2}\right)\Delta z \tag{39}$$

or

$$\phi_i(z+\Delta z) = \phi_i(z)\exp\left\{\left(g - j\pi\frac{\lambda i^2}{a_x^2}\right)\Delta z\right\} \tag{40}$$

Reconstructing the Fourier expansion yields the BPM expression for the electric field propagated one step forward in z.

$$E(x_m, z+\Delta z) = \frac{1}{\mathcal{N}_x}\sum_{i=0}^{\mathcal{N}_x-1}\phi_i(z)\exp\left\{\left(g - j\pi\frac{\lambda i^2}{a_x^2}\right)\Delta z\right\}e^{j2\pi\frac{nm}{\mathcal{N}_x}} \tag{41}$$

The next step is to establish the connection between the complex amplitude gain function g and the local carrier concentration N. For this model a phenomenological approach is taken in which the optical power gain coefficient G is assumed to vary linearly with the local carrier concentration with constant of proportionality A.

$$G = A(N - N_{tr}) \tag{42}$$

where N_{tr} is the carrier concentration required for transparency. The carrier induced change in refractive index, Δn_c, is assumed to have the same form so that Δn_c, is proportional to G with proportionality constant

$$\alpha = 2k_0\frac{\frac{dn}{dN}}{\frac{dG}{dN}}, \tag{43}$$

which is the anti-guiding or linewidth enhancement factor with k_0 being the free space wave number.

The power gain coefficient G in an amplifying medium with imaginary susceptibility χ_c'' is $G = -k\chi_c''$. To relate Δn_c to the real susceptibility χ_c' we first rewrite Eq.(22).

$$\mathcal{D} = \epsilon_0 n^2(1 + \chi_c' + j\chi_c'')\mathcal{E} \tag{44}$$

From this we can see that the total refractive index must be

$$\begin{aligned} n_{tot} &= n + \Delta n_c \\ &= \sqrt{n^2(1+\chi_c')} \\ &\approx n\left(1 + \frac{\chi_c'}{2}\right), \end{aligned} \tag{45}$$

which implies that $\Delta n_c = n\frac{\chi_c'}{2}$ where we have used the fact that the carrier induced portion of the real susceptibility is small enough to Taylor expand the square root. We can now rewrite Eq.(32) in terms of G using Eq.(43).

$$g = \Gamma\frac{G}{2}(1 + j\alpha) - a \tag{46}$$

Finally, Eq.(41) becomes

$$E(x_m, z + \Delta z) = e^{\left\{\Gamma\frac{G}{2}(1+j\alpha)-a\right\}\Delta z}\frac{1}{\mathcal{N}_x}\sum_{i=0}^{\mathcal{N}_x-1}\phi_i(z)e^{j\pi\left\{\frac{2nm}{\mathcal{N}_x} - \frac{\lambda_i^2\Delta z}{a_x^2}\right\}} \tag{47}$$

This allows us to propagate a beam through a semiconductor medium with gain G specified in terms of the carrier concentration by Eq.(42). Propagation is simulated by first taking the FFT of electric field profile at the input plane, multiplying the $\phi_i(z)$ by the phase factor given in Eq.(47), taking the inverse FFT of the $\phi_i(z)$, and then multiplying by the complex gain factor in Eq.(47). To complete the simulation we must now find a solution for the carrier concentration N everywhere in the amplifier active region.

Solving for the Carrier Concentration

The carrier concentration in the amplifier active region is modeled by a standard carrier diffusion rate equation as can be found in reference [70]. Simplifications are made to reduce the rate equation to a linear second order ordinary differential equation that is then converted to finite difference equations that are solved by matrix inversion. The carrier diffusion rate equation is

$$D_e\nabla^2 N(x,z) + \frac{\eta_i J(x,z)}{eW_a} - R = 0 \tag{48}$$

where D_e is the effective diffusion constant, η_i the injection efficiency, J is the injected current density, e the electronic charge, W_a the thickness of the carrier confining quantum well region, and R is the total rate of recombination due to all mechanisms. Again, these parameters are summarized in Table (2). We will neglect spontaneous emission, Auger recombination, and all other terms in R of greater than first order in N and consider only stimulated emission and first order non-stimulated recombination such that

Table 2. Summary of Parameters Used in FFT BPM Simulation

Symbol	description	typical value	
D	BAL width	400	μm
$\mathcal{N}_x$	# mesh points in x	1024	
Δ	mesh spacing in x	0.5	μm
Δz	mesh spacing in z	10	μm
a_x	periodic window	512	μm
n	background refractive index	3.7	
λ	wavelength	0.833	μm
k	wave number	$\frac{2\pi n}{\lambda}$	
Γ	confinement ratio	0.011	
$\hbar\omega$	photon energy	2.386×10^{-19}	Joules
Z_0	wave impedance	$\frac{377}{n} \approx 100$	Ω
A	phenomenological gain constant	3.3×10^{-8}	μm^2
N_{tr}	transparency carrier density	1.75×10^6	μm^{-3}
D_e	effective diffusion constant	25×10^8	$\frac{\mu m^2}{s}$
τ	non-stimulated lifetime	2.5	ns
η_i	injection efficiency	0.90	
e	electronic charge	1.602×10^{-19}	Coulombs
α	anti-guiding parameter	2.5	
a	non-saturable cladding loss	3.5×10^{-4}	μm^{-1}
W_a	active region thickness	10	nm
R_2	back facet reflectivity	0.9	

$$R = \frac{\Gamma G}{\hbar\omega} I(x,z) + \frac{1}{\tau} N(x,z) \tag{49}$$

where

$$I(x,z) = \frac{1}{Z_0} \, |E(x,z)|^2 \tag{50}$$

is the total optical intensity at the point (x,z), $\hbar\omega$ is the photon energy, and τ is the lifetime of carriers against all non-stimulated first order recombination mechanisms.

Transverse (y directed) diffusion can be neglected since the charge carriers of interest are well confined in the narrow quantum well active region. Longitudinal (z directed) diffusion is caused by two sources of saturation induced carrier concentration variation. The first is the slowly varying longitudinal carrier profile caused by the amplification of the traveling waves in the cavity. This varies over a scale much larger than the diffusion length and can thus be neglected. The second is the quickly varying spatial hole burning pattern caused by interference between the forward and backward traveling waves in the cavity. This varies over a scale on the order of an optical wavelength which is much shorter than the diffusion length and hence is quickly washed out by diffusion. In addition, this longitudinal spatial hole burning is predictable and fairly well understood and not the feature of interest in this study. Hence the Laplacian operator in Eq.(48) can be replaced by the one-dimensional second order derivative in x. This reduces Eq.(48) to a linear second order ordinary differential equation.

$$D_e \frac{\partial^2 N}{\partial x^2} - \frac{1}{\tau} N - \frac{A\Gamma}{\hbar\omega}(N - N_{tr}) I + \frac{\eta_i J}{e W_a} = 0, \tag{51}$$

which has the form

$$\frac{\partial^2 N}{\partial x^2} = pN + q \tag{52}$$

where p and q are given by

$$p = \frac{1}{D_e \tau} + \frac{\Gamma A I}{D_e \hbar\omega} \tag{53a}$$

$$q = -\frac{\Gamma A I N_{tr}}{D_e \hbar\omega} + \frac{\eta_i J}{D_e e W_a}. \tag{53b}$$

When we discretize x and impose the boundary condition of zero carrier concentration outside of the pumped region Eq.(51) becomes the following set of finite difference equations:

$$\begin{array}{rlll} N_{k+1} - (2 + \Delta^2 p_k) N_k + N_{k-1} & = \Delta^2 q_k & \text{for} & 1 \le k \le \mathcal{N}_x \\ N_1 - (2 + \Delta^2 p_0) N_0 & = \Delta^2 q_0 & \text{for} & k = 0 \\ -(2 + \Delta^2 p_{\mathcal{N}_x - 1}) N_{\mathcal{N}_x - 1} + N_{\mathcal{N}_x - 2} & = \Delta^2 q_{\mathcal{N}_x - 1} & \text{for} & k = \mathcal{N}_x - 1 \end{array} \tag{54}$$

where Δ is the mesh spacing in the x direction and $N_k = N(x = k\Delta)$ and similarly for p and q. This set of $\mathcal{N}_x$ linear equations can be expressed as a tridiagonal matrix equation.

$$\begin{bmatrix} c_0 & 1 & 0 & \dots & 0 & 0 & 0 \\ 1 & c_1 & 1 & & & & 0 \\ 0 & 1 & c_2 & & & & 0 \\ \vdots & & & \ddots & & & \vdots \\ 0 & & & & c_{\mathcal{N}_x-3} & 1 & 0 \\ 0 & & & & 1 & c_{\mathcal{N}_x-2} & 1 \\ 0 & 0 & 0 & \dots & 0 & 1 & c_{\mathcal{N}_x-1} \end{bmatrix} \cdot \begin{bmatrix} N_0 \\ N_1 \\ N_2 \\ \cdot \\ \cdot \\ \cdot \\ N_{\mathcal{N}_x-1} \end{bmatrix} = \Delta^2 \begin{bmatrix} q_0 \\ q_1 \\ q_2 \\ \cdot \\ \cdot \\ \cdot \\ q_{\mathcal{N}_x-1} \end{bmatrix}, \tag{55}$$

where $c_k = -(2 + \Delta^2 p_k)$. This simulation solves equation Eq.(55) using a standard technique for inverting a tridiagonal matrix. This procedure is applied to each row of the problem mesh to give the carrier concentration at each mesh point for a given electric field distribution.

Convergence Procedure

The two halves of the simulation described in the preceding two sections are allowed to interact in a simple iterative loop until the solutions converge to a steady state. The simulation accepts as input the injected spotsize, injected power, angle of injection, location of injected beam center, and the bias current density. The injected beam is assumed to be Gaussian and the bias current density is assumed to be uniform over the pumped region and zero elsewhere.

Fig.(3.7) illustrates the convergence procedure used. First the unsaturated carrier concentration induced by the uniform injection current is calculated for the entire device using the procedure described in the last section. Then the input Gaussian profile is propagated using Eq.(47) across the problem mesh to the back facet storing the value of the electric field at each mesh point. The carrier concentration as saturated by the forward propagating wave is then calculated. Next the back facet reflectivity is applied and the backward travelling wave is propagated back across the device and stored. The simulation then enters the main convergence loop in which the carrier concentration is calculated based on the ith estimate of the fields and then the $(i + 1)$th estimate of the fields are obtained by propagating the Gaussian input forward and then backward across the device. Then, if the fields have not converged, the loop repeats.

The convergence error at each mesh point corresponding to the ith iteration is defined as

$$\delta = \frac{|I^i - I^{i+1}|}{I^i + I^{i+1}} \tag{56}$$

so that $0 \leq \delta \leq 1$. A maximum convergence error is defined as δ_{max} (usually $\delta_{max} = 10^{-5}$) and iteration is continued until

$$\max_{\{x,z\}}(\delta) < \delta_{max} \tag{57}$$

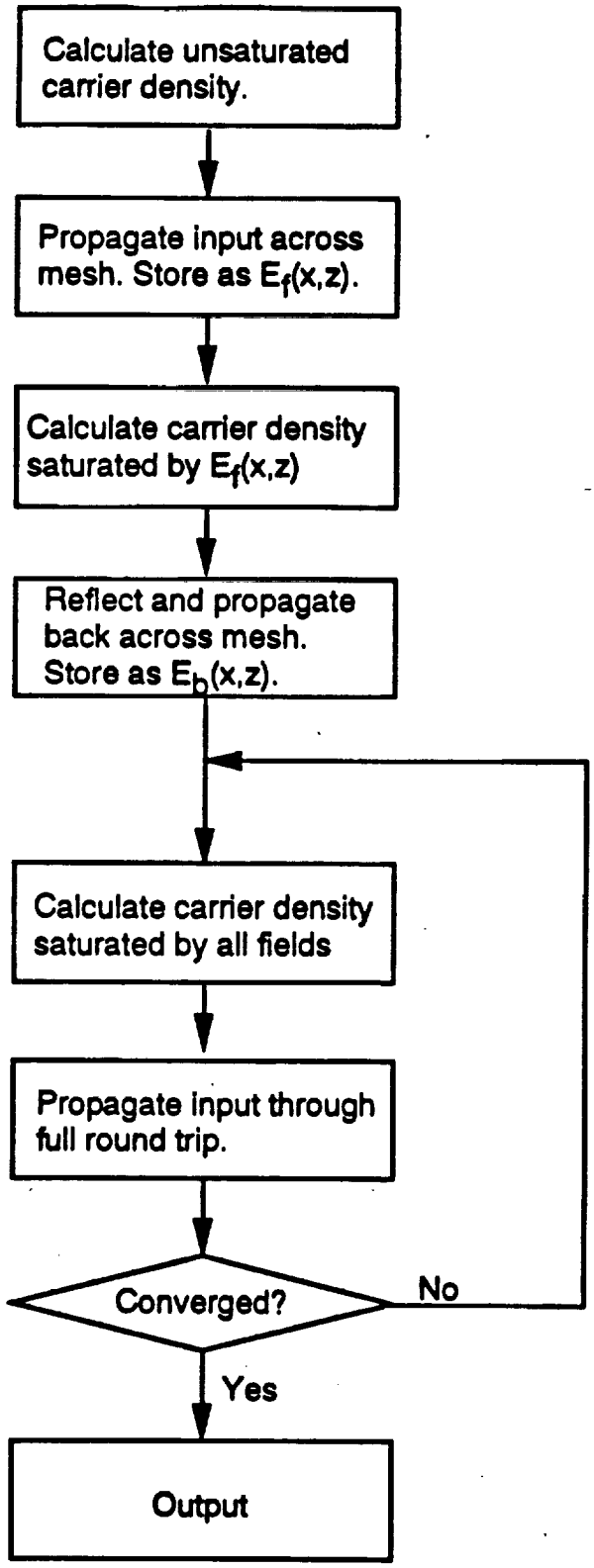

Figure 3.7: Illustration of simulation convergence procedure.

where the maximum is taken over both forward and backward propagating waves. At this point a self-consistent solution to the paraxial wave equation and the carrier diffusion rate equation has been found.

The output of the simulation consists of all of the stored field and carrier concentration profiles and some resulting calculated data. The near-field emission of the amplifier is taken to be the calculated profile of the backward travelling wave at $z = 0$ ($E_b(x, z = 0)$). The output power and total power gain can also be calculated from this profile. The far-field pattern as a function of far-field angle $\Theta \equiv \frac{x}{r}$ at some large distance r is calculated using the Fraunhofer integral over the near-field.

$$E_{ff}(\Theta) = \frac{j}{r\lambda} e^{jkr} \int_0^{a_x} E_b(x', z = 0) e^{jk\Theta x'} dx' \tag{58}$$

which, when discretized for calculation, becomes

$$E_{ff}(\Theta_m) = \frac{j}{r\lambda} e^{jkr} \Delta \sum_{i=0}^{\mathcal{N}_x - 1} E_b(x_i, z = 0) e^{\frac{j2\pi mi}{\mathcal{N}_x}} \tag{59}$$

where $\Theta_m \equiv \frac{\lambda m}{a_x}$ is the discretized far-field angle. This simulation was implemented in a C++ computer program which was executed on a Sun Microsystems Sparkstation IPC computer. The predicted results of this simulation are given in the next section.

Predicted Results of the FFT BPM Model

The FFT BPM model described above has been applied to a $400\mu m$ wide by $500\mu m$ long double pass reflective travelling wave amplifier. This configuration was chosen to allow comparison to the recent experimental results reported by Goldberg and Weller (see Table(1) [25]. The AlGaAs amplifier in this experiment was a separate confinement single quantum well device with a $100\mathring{A}$ wide well and a confinement factor of $\Gamma = 0.05$. The back facet was coated for high reflectivity at the operating wavelength of 820nm and the front facet was anti-reflection coated to an estimated reflectivity of $R_1 \approx 0.5 - 1\%$. The injected signal came from a tunable Ti:sapphire laser and the system was operated under pulsed conditions with a $0.5\mu s$ pulse length and a 10% duty cycle. The model, of course, assumes that the fields and carrier concentration in the amplifier reach steady state during the pulse.

Figs.(3.8),(3.9),(3.10), and (3.11) show the predicted model results for four different operating conditions. In Fig.(3.8) the amplifier was biased at 3.5A and injected with 350 mW of master oscillator light. Fig.(3.9) shows the result with 3.5 A and only 1mW input power. In Fig.(3.10) 350mW of optical power was injected into the amplifier biased at 1.1A and in Fig.(3.11) 1.1A and 1mW were used. In all four figures the input beam was taken to be a Gaussian beam with full width at half maximum power of $200\mu m$ injected at a 5° external angle of incidence. The figures show the near-field distribution on the bottom, far-field profile on the top and the profile of the amplitude gain coefficient at the front facet in the center.

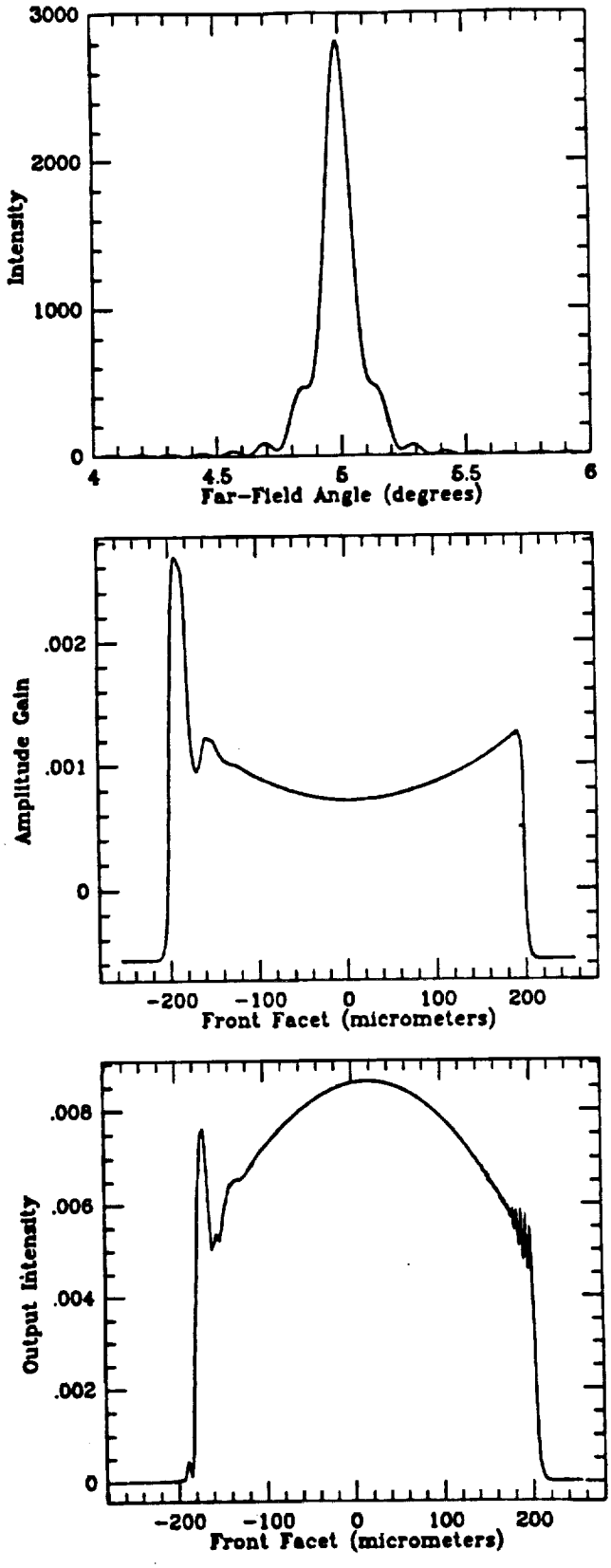

Figure 3.8: Near-Field (bottom), Gain (center), and Far-Field (top) Profiles. Bias Current: 3.5A. Injected Power: 350mW.

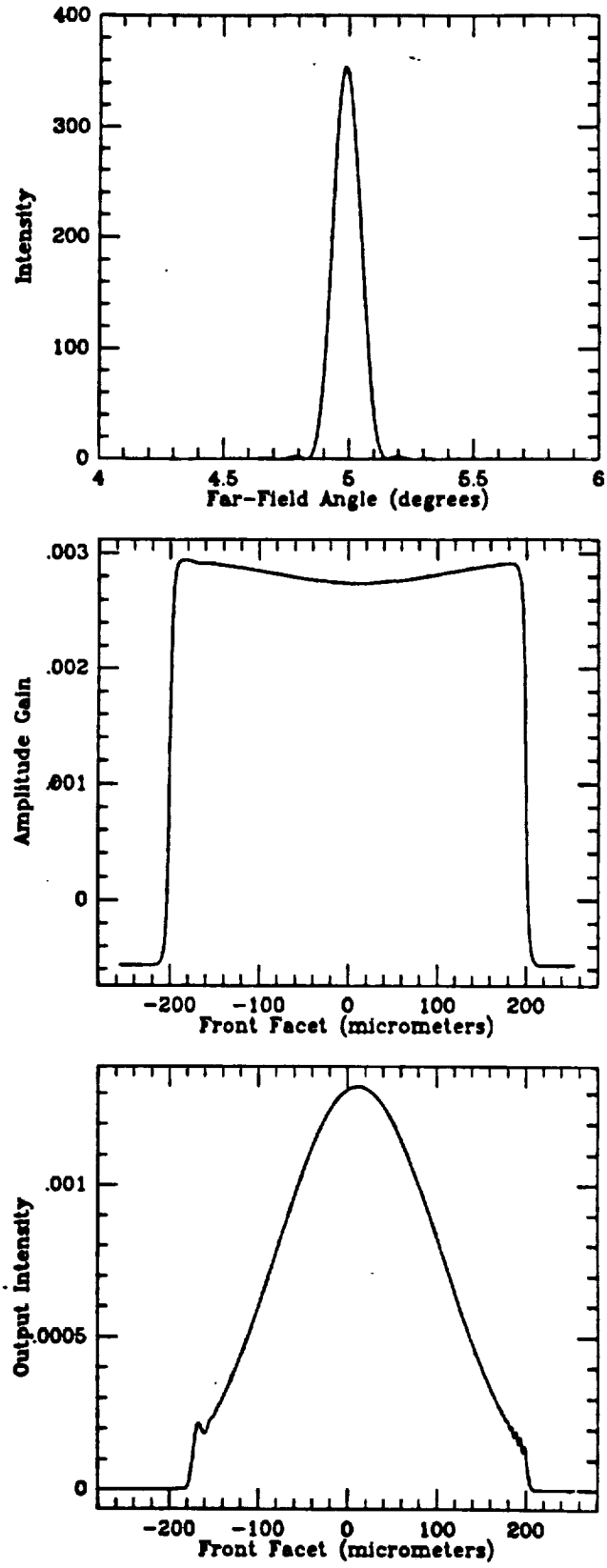

Figure 3.9: Near-Field (bottom), Gain (center), and Far-Field (top) Profiles. Bias Current: 3.5A. Injected Power: 1mW.

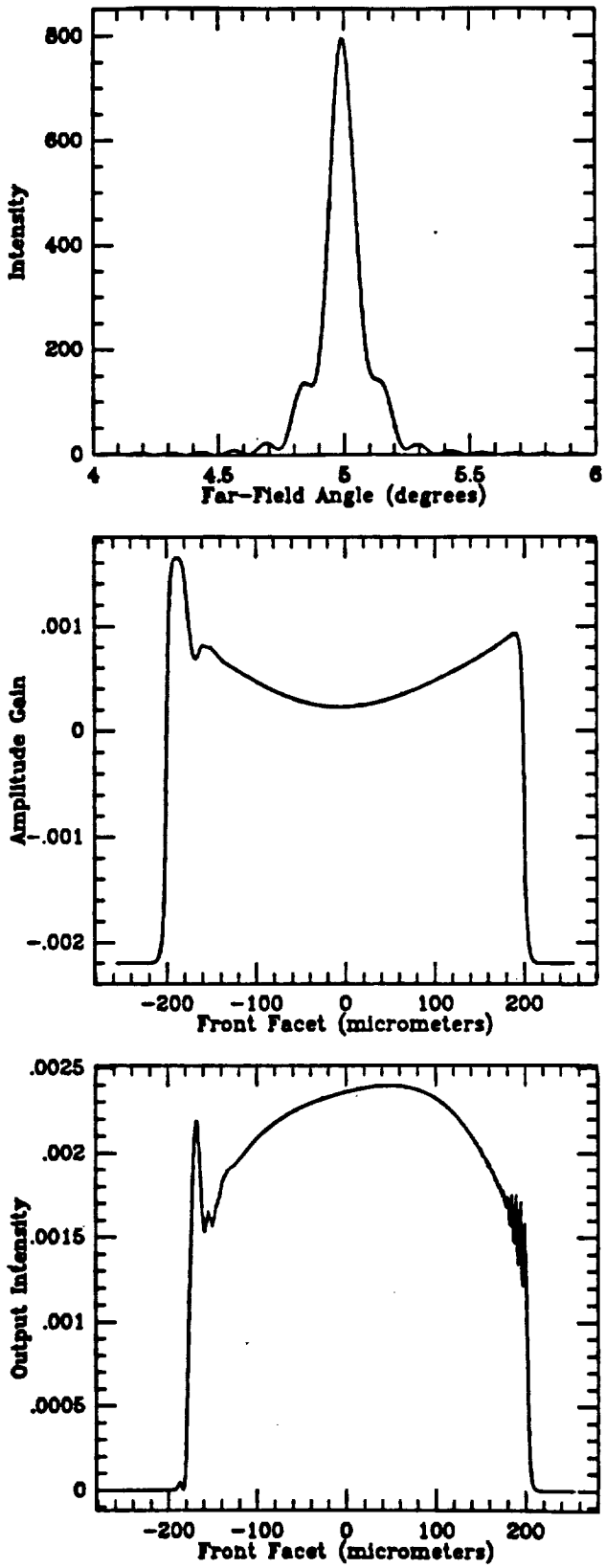

Figure 3.10: Near-Field (bottom), Gain (center), and Far-Field (top) Profiles. Bias Current: 1.1A. Injected Power: 350mW.

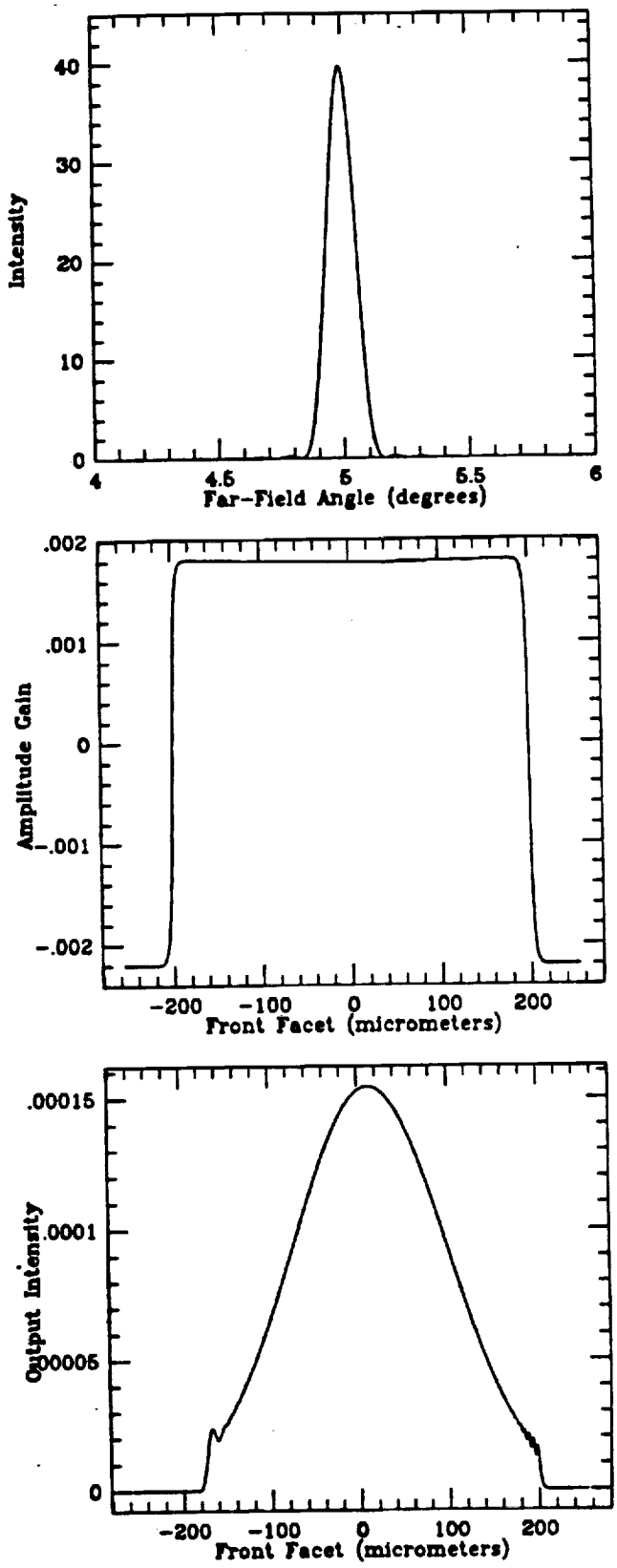

Figure 3.11: Near-Field (bottom), Gain (center), and Far-Field (top) Profiles. Bias Current: 1.1A. Injected Power: 1mW.

For the run of Fig.(3.11) an output power of 32.4mW was predicted for a gain of 15.1dB. The corresponding measurement from reference [25] gave a power gain of 15.2dB. The run at 1.1A and 350mW predicted an output of 807mW which corresponds to a strongly saturated gain of only 3.6dB. The Goldberg data also shows 807mW output. The largest gain was achieved for 3.5A and 1mW (Fig.(3.9)) which produced 24.6dB or 286mW output power. When the input power was increased to 350mW the gain at 3.5A was reduced to 9.1dB. The Experimental data showed 25dB and 8.5dB, respectively, for those two cases. The structure of the far-field profile in Fig.(3.8) compares well to the experimental far-field measurement given in reference [25] although the experimental far-field shows less symmetry in the side lobe structure. According to the modeling results given in reference [16], this asymmetric structure may be the result of regenerative effects due to residual front facet reflectivity which is neglected in the present model.

An important feature to note in these four figures is the degree of spatially non-uniform gain saturation. In the low current, low input power case of Fig.(3.11) the gain shows very little saturation and is nearly uniform across the front facet profile shown. When the current is increased to 3.5A (Fig.(3.9) the gain profile becomes noticeably non-uniform with a central dip and nearly unsaturated edges. This is because the small input signal is amplified much more strongly at the high current and hence more optical power is available to saturate the gain. If the current is kept low (1.1A) and a large input signal is used the gain is much more strongly saturated, as seen in Fig.(3.10). This figure also shows a spike in the gain profile at the left edge of the facet which is where the input beam was incident. In this region, only the outer edge of the high power amplified beam was present to saturate the gain, hence the gain here remains large. This also leads to a corresponding spike in the near-field profile. The highest power run at 3.5A and 350mW (Fig.(3.8)) also shows the largest degree of saturation with the gain in the beam center reduced to almost zero and the gain spike remaining on the left edge.

The impact of the non-uniform gain saturation on the near-field and far-field profiles is also evident in the figures. The central dip in the gain profile causes the edges of the amplified beam to experience more total gain than its center. As a result, the contrast ratio of the intensity at beam center to the intensity at the edges is significantly reduced. In the low power runs, Figs. (3.11) and (3.9), this ratio was 11.9 and 11, respectively. In the high power runs, however, the contrast ratio was reduced to 1.7 and 1.8 for Figs.(3.10) and (3.8), respectively. The edge intensity for the calculation of the contrast ratio was taken at the far right edge of the figures. This reduction of the contrast between intensities at the beam's edge and at its center results in an enhancement of the side lobes in the corresponding far-field patterns. The near-field for the low power cases is still nearly Gaussian and, hence, so is the far-field. In the high power cases, however, the near-field is more nearly uniform and the far-field is therefore similar to the diffraction pattern that one would expect from a uniformly illuminated slit.

Fig.(3.12) shows another interesting prediction of the FFT BPM model that agrees well with experimental observation. It has been observed both in experiments and other simulations that high power MOPA systems exhibit strong near-field filamentation and corresponding degradation of the far-field when the master oscillator beam is injected at normal

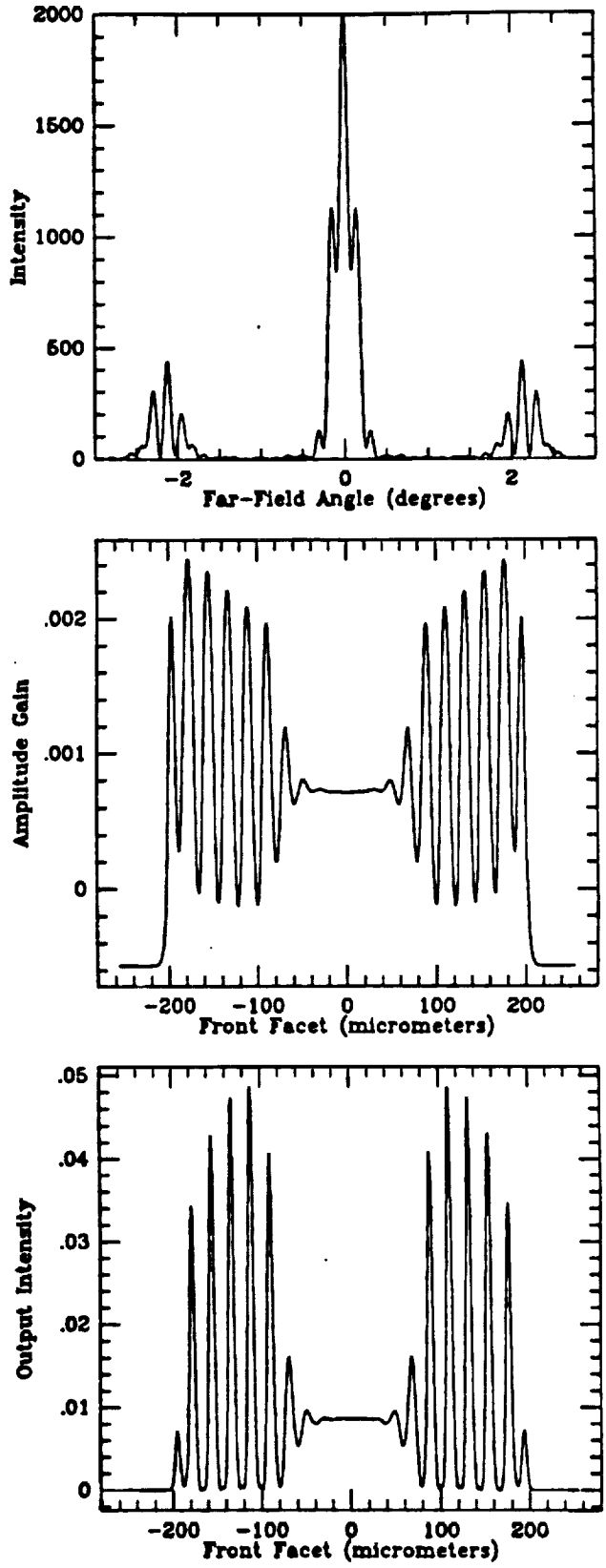

Figure 3.12: Near-Field (bottom), Gain (center), and Far-Field (top) Profiles. Bias Current: 3.5A. Injected Power: 350mW. Angle of Incidence: 0°.

incidence with the facet [16]. This is a complex nonlinear effect thought to be related to carrier induced self focusing. Typically the filamented near-field structure is unstable and shifting in time, not reaching steady state. When the FFT BPM model is run with a normally incident injected beam, the resulting near-field and far-field patterns also show the expected filamentation. Fig(3.12) was run under the same conditions as Fig.(3.8) except that the injected beam was normally incident. The run never converged to a self-consistent solution, which is to be expected since the experimentally observed filamentation is not steady state. In addition to near-field filamentation and far-field degradation, Fig.(3.12) also shows the corresponding spiking of the lateral gain profile. This also implies spiking of the refractive index profile according to Eq.(46), which causes filamented self focusing.

An important point needs to be made about the limitations of the FFT BPM model as it has been presented. In order to linearize the carrier diffusion rate equation (Eq.(51)) and simplify the calculations, spontaneous emission and other non-linear recombination mechanisms were neglected. In addition, the model does not account for transverse lasing in the amplifier cavity. As a result, the unsaturated small signal gain predicted by the model is much larger than actually observed in experiment. If we ignore diffusion and stimulated emission, the unsaturated carrier concentration can be calculated from Eq.(51). The result is

$$N = \frac{\tau \eta_i J}{e W_a} \tag{60}$$

which is linear in the injected current J. Therefore the total gain in decibels due to these carriers is also linear in the current. In reference [25], however the small signal gain is seen to saturate at high current. The very high small signal gain given by this linear model causes the first estimate of the field intensities in the convergence iterations to be very much larger than the realistic value. This results in a very slowly converging solution. In order to achieve proper convergence in a reasonable amount of time in the results described above the phenomenological constants of the model (A, N_{tr}, and a) had to be adjusted such that the predicted small signal gain matched the experimentally observed value given by Goldberg and Weller.

Goldberg and Weller attribute the saturation of the small signal gain to ASE and transverse lasing [25]. Our model, however, shows that at high current the 1mW signal used in the experiment to measure small signal gain is itself an important source of gain saturation. Hence, the small signal gain reported in reference [25] is not actually the unsaturated gain, but in fact the small amplified beam experiences significant self saturation. Fig.(3.13) shows the small signal gain versus injection current for this amplifier. The top curve is the linear characteristic predicted by Eq.(60) and also predicted by the FFT BPM model without saturation effects. The bottom curve is the small signal gain measured by Goldberg and Weller in reference [25]. The center curve shows the self-consistently predicted gain versus current characteristic including saturation effects. From this figure it is evident that self saturation by the 1mW input signal does contribute to the nonlinear nature of the small signal gain. However, the predicted gain is still larger than that observed in experiment. A useful enhancement to the FFT BPM model that will better predict the nonlinear small signal gain characteristic is the inclusion of ASE saturation effects. A

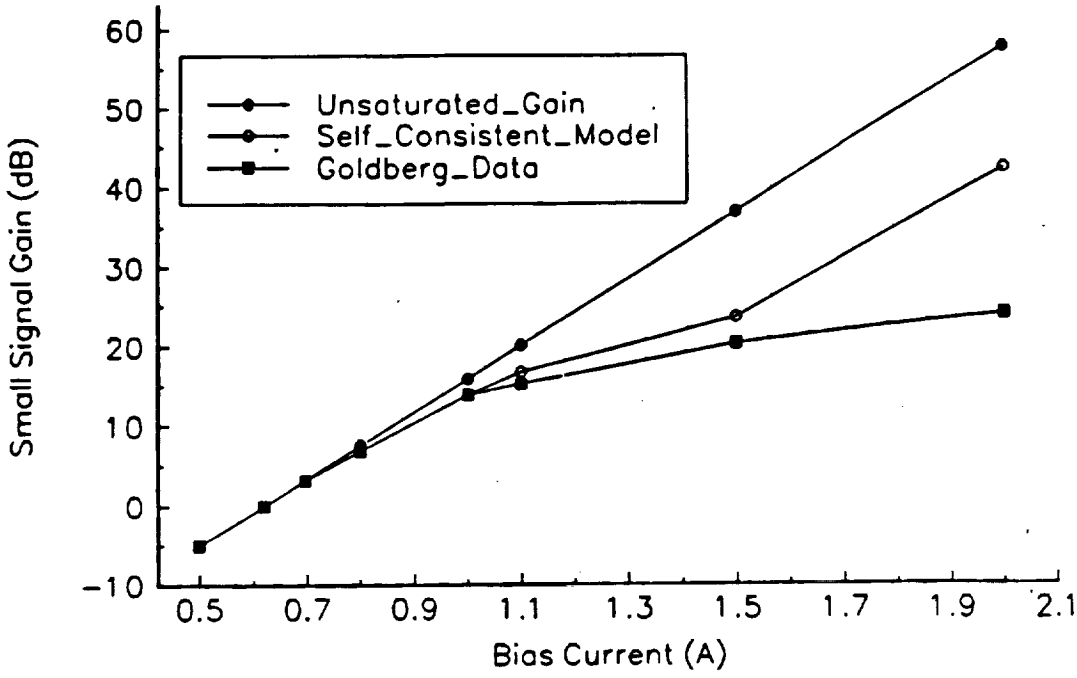

Figure 3.13: Small Signal Gain Characteristics.Top: linear model. Center: self-consistent, self-saturated model result. Bottom: experimental data from reference [25].

simple approach to including ASE effects in the FFT BPM model is given in the following section.

A Simple Model for ASE Effects in the FFT BPM Model

The underlying approach of this simple ASE model is to find an effective monochromatic field that can be propagated through the amplifier in the same way as the injected signal (Eq.(47)) which will approximate the effect of ASE induced gain saturation. The recombination of carriers due to the actual spontaneous emission, which would appear as a quadratic term in the rate equation (Eq.(51)), is not modeled since it has been observed (reference [16]) that the stimulated emission caused by ASE is a much larger effect. The difficulty is that the FFT BPM model is strictly a monochromatic model whereas spontaneous emission from a semiconductor laser diode is broadband radiation which is not easily modeled by a monochromatic field. The approach taken here is to find an effective monochromatic field whose intensity reduces the small signal gain experienced by the model's monochromatic injected field by the same amount that broadband spontaneous emission reduces the gain experienced by a narrow band injected signal.

Mathematical Development of the ASE Model

The first step is to return to Eq.(51) to find an expression for the gain saturated by a monochromatic signal. We first define the effective inversion density as

$$N_e = N - N_{tr} \tag{61}$$

so that the phenomenological gain of Eq.(42) becomes simply $G = AN_e$. Then, after neglecting diffusion, Eq.(51) can easily be solved to see that

$$N_e = \frac{N^0}{1 + \frac{I}{I_{sat}}} \tag{62}$$

where

$$N^0 = \frac{\tau \eta_i J}{eW_a} - N_{tr} \tag{63}$$

is the unsaturated inversion density and

$$I_{sat} = \frac{hf}{\tau \Gamma A} \tag{64}$$

is the intensity at which the N_e is reduced to half of its unsaturated value. Thus the amplitude gain coefficient experienced by a monochromatic beam in a medium saturated by spontaneous emission of intensity I_{sp} is

$$g_{ms} = \Gamma A N_e = \frac{\Gamma A N^0}{1 + \frac{I_{sp}}{I_{sat}}}. \tag{65}$$

Next we need to estimate the gain seen by a narrowband optical signal in a broadband amplifier saturated by broadband spontaneous emission. To do this we write a rate equation analogous to Eq.(51) with the inclusion of a simple spectral dependence. The inversion

density, pumping rate and spontaneous emission are assumed to be characterized by the same lineshape function, $g_a(f)$, which is taken to be the uniform distribution over the amplifier bandwidth, Δf_a. The intensity in the cavity is allowed to have some other spectral dependence $I(f)$. The rate equation is

$$P_0 g_a(f) - \frac{N}{\tau} g_a(f) - \frac{\lambda^2}{8\pi} A_E N_e g_a(f) \frac{I(f)}{hf} = 0 \tag{66}$$

where P_0 is the effective pumping rate at line center and A_E is the Einstein spontaneous emission coefficient from semi-classical laser theory. Diffusion has again been neglected in Eq.(66). This equation is easily solved to find an expression analogous to Eq.(62).

$$N_e = \frac{N_f^0}{1 + \frac{I(f)}{I_{sat,f}}} \tag{67}$$

where

$$N_f^0 = P_0 \tau - N_{tr} \tag{68}$$

and

$$I_{sat,f} = \frac{8\pi hf}{A_E \lambda^2 \tau} \tag{69}$$

are analogous to N^0 and I_{sat} above. The gain coefficient at frequency f is then

$$\gamma_s(f) = \frac{\lambda^2}{8\pi} A_E g_a(f) N_e = \frac{\lambda^2}{8\pi} A_E g_a(f) \frac{N_f^0}{1 + \frac{I(f)}{I_{sat,f}}} \tag{70}$$

If we now let the saturation inducing intensity in Eq.(70) be the broadband spontaneous emission from the carriers in one longitudinal mesh spacing of the form

$$I(f) = A_E N g_a(f) hf \Delta z \tag{71}$$

then the total gain coefficient experienced by a small injected signal with narrow lineshape $\xi(f)$ is

$$g_s = \int_{-\infty}^{\infty} \gamma_s(f) \xi(f) df = A_E \frac{\lambda^2}{8\pi} \frac{N_f^0}{\Delta f_a + A_E^2 N_e \frac{\lambda^2 \tau}{8\pi} \Delta z} \tag{72}$$

where $\xi(f)$ is taken to be the uniform distribution over the bandwidth of the master oscillator signal.

We next need to relate the Einstein coefficient A_E to the phenomenological constants of the FFT BPM model. To do this, we return to Eq.(66) and, letting $I(f) = I_{mo}\xi(f)$ be the master oscillator intensity, we integrate over all frequencies to arrive at

$$P_0 - \frac{N}{\tau} - \frac{c^2 I_{mo}}{8\pi h f^3 \Delta f_a} A_E N_e = 0 \tag{73}$$

By comparison to Eq.(51) we can now see that

$$P_0 = \frac{\eta_i J}{eW_a} \tag{74}$$

and, more importantly,

$$A_E = \frac{8\pi\Delta f_a}{\lambda^2}\Gamma A \tag{75}$$

Now we can find the effective monochromatic spontaneous emission intensity that we seek by using Eq.(75), letting $g_{ms} = g_s$, and solving for I_{sp}. The result is

$$I_{sp} = \hbar\omega\frac{8\pi}{\lambda^2}\Delta f_a \Delta z \Gamma G \tag{76}$$

The model will assume that all of the spontaneous emission from a block of gain is concentrated on the corresponding mesh point. The emission from a mesh point is assumed to be at a random time, and hence have random phase, and to radiate in all directions uniformly. From a given mesh point, (x, z), half of the spontaneous emission power will propagate forward and half will propagate backward. Of the half traveling in either direction, only a fraction will be guided by the transverse direction laser waveguide structure. If Θ' is the critical angle of internal reflection at the transverse waveguide interface then the fraction, F, of the power that is guided can be estimated by

$$F = \frac{1}{4\pi}\int_0^{2\pi}\int_{\frac{\pi}{2}-\Theta'}^{\frac{\pi}{2}+\Theta'} \sin\Theta d\Theta = \cos(\arcsin\frac{n_{clad}}{n}) \tag{77}$$

The model also considers only that portion of the spontaneous emission power propagating in a given direction that will arrive at the nearest laser facet before leaving the pumped gain region. This is justified since only this portion of the wave is amplified to a sufficient degree to significantly saturate the gain. This assumption is therefore most valid for traveling wave amplifiers that are longer than they are wide. If Θ_1 and Θ_2 are the angles between the longitudinal axis and the lines between a point (x, z) and the edges of the nearest facet (see Fig.(3.14)) then the included fraction of the power is estimated to be

$$\frac{\Theta_1 + \Theta_2}{2\pi} \tag{78}$$

With these considerations, the net spontaneous emission intensity traveling in either direction (Eq.(76)) becomes

$$I_{sp} = \frac{\Theta_1 + \Theta_2}{2\pi} F\hbar\omega\frac{8\pi}{\lambda^2}\Delta f_a \Delta z \Gamma G \tag{79}$$

The electric field that produces this intensity is taken to be an integral of randomly phased, off-axis plane waves over all propagation angles between Θ_1 and Θ_2.

$$\begin{aligned}\mathbf{E}_{sp}(x,z) &= E_0(x,z)\int_{-\Theta_1}^{\Theta_2} e^{jk(\cos\Theta z + \sin\Theta x) + j\phi'_{rand}}(\cos\Theta\hat{x} - \sin\Theta\hat{z})d\Theta \\ &= E_0(x,z)e^{\phi_{rand}}\left[(\sin\Theta_1 + \sin\Theta_2)\hat{x} + (\cos\Theta_2 - \cos\Theta_1)\hat{z}\right],\end{aligned} \tag{80}$$

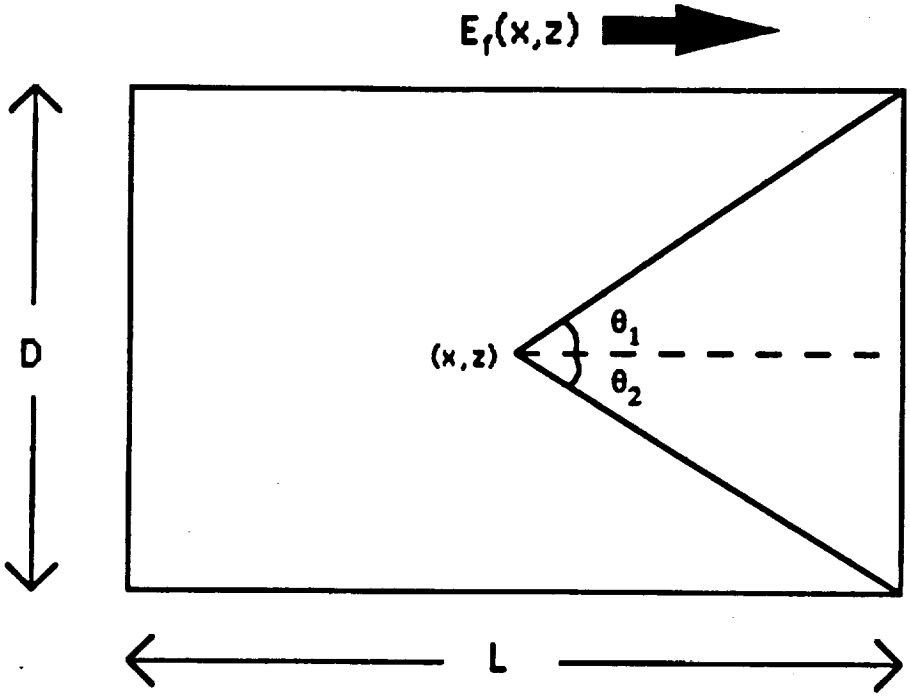

Figure 3.14: Sketch showing arrangement and parameters in the spontaneous emission model.

where $\hat{x}$ and $\hat{z}$ are unit vectors and since ϕ'_{rand} is random, the total phase is random and assumed to be uniform on 0–2π at each point (x, z). Hence the phase term can be removed from the integral.

The intensity corresponding to this wave is

$$\begin{aligned}\frac{|\mathbf{E}_{sp}(x,z)|^2}{Z_0} &= \frac{|E_0(x,z)|^2}{Z_0}\left[(\sin\Theta_1+\sin\Theta_2)^2+(\cos\Theta_2-\cos\Theta_1)^2\right] \\ &= \frac{|E_0(x,z)|^2}{Z_0}2(1-\cos(\Theta_1+\Theta_2))\end{aligned} \tag{81}$$

where a standard trigonometric identity has been used.

We then set Eq.(81) equal to Eq.(79) and solve for $E_0(x, z)$

$$E_0(x,z) = \sqrt{\frac{2FZ_0(\Theta_1+\Theta_2)\hbar\omega\Delta z G(x,z)}{\lambda^2\left[1-\cos(\Theta_1+\Theta_2)\right]}} \tag{82}$$

We take only the x directed component for the scalar FFT BPM and hence arrive at the final expression for the effective spontaneous emission source field.

$$E_{sp}(x,z) = \sqrt{\frac{2FZ_0\hbar\omega\Delta z}{\lambda^2}}\sqrt{\frac{(\Theta_1+\Theta_2)G(x,z)}{1-\cos(\Theta_1+\Theta_2)}}(\sin\Theta_1+\sin\Theta_2)e^{j\phi_{rand}} \tag{83}$$

This field was incorporated into the FFT BPM model by propagating it through the amplifier using Eq.(47) at each iteration of the convergence loop and including the corresponding ASE intensity in the calculation of the saturated gain. The results of this enhancement of the FFT BPM model will be discussed in the following section.

Predicted Results of the FFT BPM Model with ASE Effects

The simple approach for inclusion of ASE effects in the FFT BPM model described in the previous section proved to be successful at modeling the ASE induced saturation of the total amplifier gain. However, the predicted spatial detail of the near-field and far-field profiles require critical interpretation. Fig(3.15) demonstrates the influence of ASE induced saturation on the overall small signal gain of the $400\mu m$ by $500\mu m$ amplifier modeled earlier. This figure is similar to Fig.(3.13) except for the addition of the predicted small signal gain including ASE. For clarity, the experimental results have been plotted as unconnected data points. Once again, the top curve shows the linear dependence of the unsaturated gain on injection current. The second curve from the top is the self-consistently computed gain experienced by a 1mW injected signal as calculated by the FFT BPM model without the inclusion of ASE. The bottom connected curve is the self-consistently computed gain for the same signal using the ASE model described above. The unconnected data points are the experimental data reported by Goldberg and Weller in reference [16]. As can be seen from the figure, the predicted results match the experimental data well and represent a definite improvement over the FFT BPM model results calculated without ASE effects. Unfortunately, the large unsaturated gain seen in the first convergence iteration,

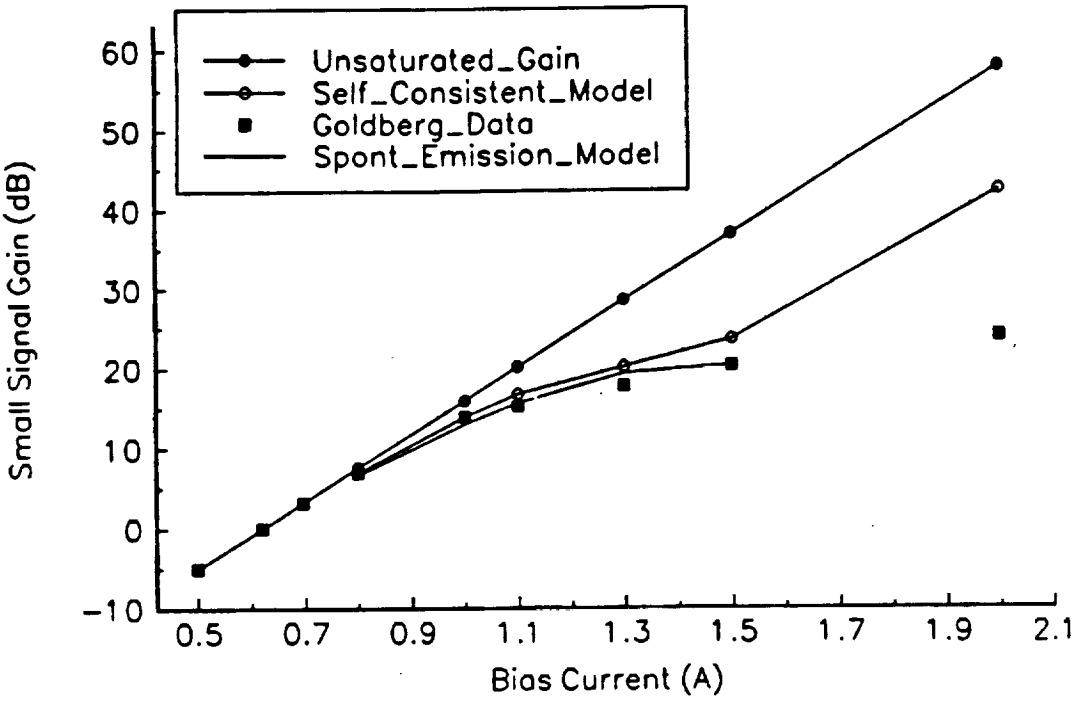

Figure 3.15: Small Signal Gain Characteristics. Top: linear model. Center: FFT BPM model without ASE. Bottom: FFT BPM model with ASE. Unconnected Points: experimental data from reference [16].

combined with the interaction of the two sets of optical fields prevented the simulation from converging to a stable solution at bias currents above 1.5A. Perhaps in future work an improved convergence proceedure will allow implementation of this model at higher bias current levels.

The predicted spatial detail of the near-field, far-field and front facet gain profiles is shown in Fig.(3.16). This run of the model used the same input conditions as Fig.(3.11) with an injected beam of 1mW and 1.1A amplifier bias current. In this figure it can be seen that the random spontaneous emission noise has caused strongly nonuniform gain saturation that has caused spatial aberration of the injected beam profile. This has also lead to some degradation of the far-field profile. While spontaneous emission noise is present in experimentally measured MOPA near-field and far-field profiles, its effect is not nearly as pronounced as in this figure. This is partly due to the fact that the random phase of the spontaneous emission at each mesh point is chosen only once by a pseudorandom number generator. When the randomly phased electric field is then propagated by Eq.(47) a correspondingly random spatial profile is produced which leads to the detailed aberration seen in Fig.(3.16). In reality, however, spontaneous emission is occurring continuously in time such that the resulting spatial intensity profile is averaged out to a smooth distribution over a time scale which is very short compared to the average carrier lifetime. Another factor is that the derivation of the effective monochromatic spontaneous emission intensity in the previous section lumps the effect of broadband spontaneous emission on the gain experienced by narrowband signal into the interaction of two monochromatic waves in a spectrally uniform gain. For this reason, the intensity of the effective monochromatic spontaneous emission should not be expected to represent the spontaneous emission intensity in an actual amplifier. Despite this limitation, the simple ASE model presented here seems to represent a useful contribution to the available techniques for modeling the behavior of high power MOPA systems.

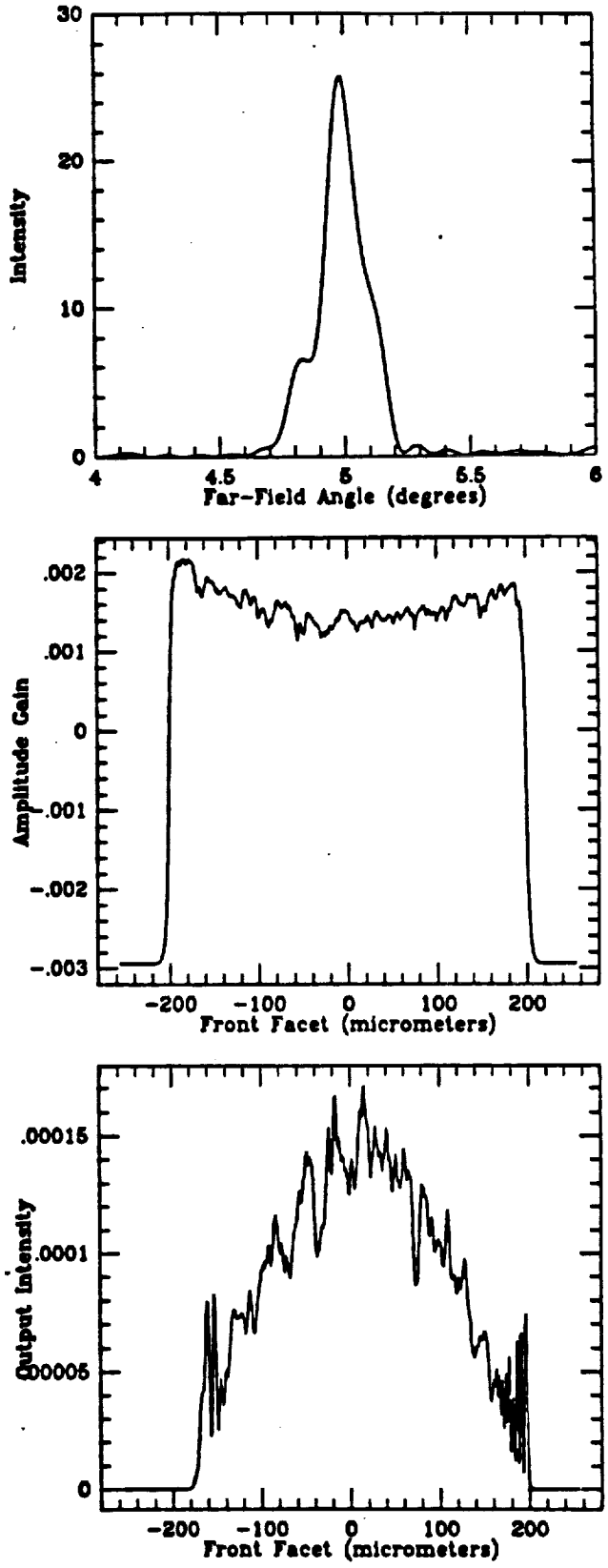

Figure 3.16: Near-Field (bottom), Gain (center), and Far-Field (top) Profiles Predicted by FFT BPM Model with ASE effects included. Bias Current: 1.1A. Injected Power: 1mW.

Conclusion

The work described here consists of the experimental investigation and numerical modeling of semiconductor laser MOPA systems. The work is in three parts. First a MOPA system using single mode fiber master oscillator coupling was built and evaluated. Second, two previously reported models, the RGBA model and the FFT BPM model, were implemented and discussed in detail. Third a new model which attempts to include the influence of ASE on MOPA system performance into the FFT BPM model was developed and implemented.

The use of an optical fiber to couple the light from the master oscillator to the power amplifier in a MOPA system was proposed as a way to reduce the size, weight, and alignment sensitivity of the system. The successful operation of such a fiber coupled MOPA has been described. The FCMOPA in this work also used a unique polarization scheme to decouple the injected master oscillator beam from the amplifier output. Single lobed near-diffraction-limited operation as well as spectral narrowing have been demonstrated. In addition, the observation of far-field beamstearing with laser diode temperature and bias current tuning was described.

The FCMOPA used miniature optical components which were expoxied together to eliminate alignment sensitive free space optical paths. The beam shaping and output decoupling optics were combined into a single unit leaving only one free space optical path just in front of the amplifier facet. The size limiting component in the optical arrangement was the optical isolator between the master oscillator and the single mode fiber. The FCMOPA suffered significant coupling losses in the miniature optics. The losses were primarily due to two factors. First, the final cylindrical lens used to focus the injected beam and collimate the amplifier output on the quickly diverging transverse axis neither adequately focused the injected beam nor efficiently captured the amplified output. Second, substitution of a $\frac{\lambda}{4}$ waveplate for the proposed Faraday rotator caused a 3dB loss of injected master oscillator power as well as a 3dB loss of decoupled amplifier output. Development of a practical FCMOPA system would require significant engineering effort to overcome these limitations.

The simple regenerative Gaussian beam amplifier model was discussed and implemented in a C++ computer program. The predicted results were found to agree quite well with the qualitative behavior of the FCMOPA system. Formation of a single lobed near-diffraction-limited far-field pattern was predicted for certain injection conditions and enhancement of the far-field was shown for large injected spotsizes. In addition, the RGBA model predicted the steering of the far-field lobe with tuning of the injected beam wavelength in a manner very similar to that observed in experiment. The RGBA model is not, however, a self-consistent solution for the optical fields in the amplifier. It neglects nonuniform gain saturation and fails to give quantitative predictions of the optical power and gain of the MOPA system.

A more sophisticated model that does solve self-consistently for the optical fields and carrier concentration in the amplifier was also implemented. The FFT BPM model used a FFT based spectral approach to solve the paraxial wave equation in conjunction with a linearized carrier diffusion rate equation. The two equations are solved iteratively until all the fields

converge to a self-consistent solution. This model does make quantitative predictions of the amplifier output power and gain as well as the field and carrier concentration profiles. Because the model assumes operation as a traveling wave amplifier with negligible front facet reflectivity, its predicted results were compared with the reported experiments on such an amplifier by Goldberg and Weller in reference [16] rather than the FCMOPA experiments reported here.

The model showed good qualitative agreement with the observed far-field patterns and served to illuminate the mechanisms by which an amplified Gaussian beam acquires a non-Gaussian side lobed profile. The simplified rate equation used in the model lead to an unsaturated amplifier gain that was much larger than observed in experiment. When the phenomenological constants of the model were adjusted to account for this effect, the model would converge with predicted quantitative gain and output power that agree well with experiment. Without this adjustment, however, the model predicted amplifier small signal gains that were significantly larger than experimentally observed. It was proposed that an enhancement to the FFT BPM model that included the gain saturation effects of amplified spontaneous emission may better match the experimental observations.

A simple approach to the inclusion of the gain saturation effects of ASE in the FFT BPM model was developed and implemented. This approach uses techniques from semi-classical laser theory along with the phenomenological treatment of the semiconductor laser medium to arrive at an effective monochromatic source field that simulates the behavior of ASE in the amplifier. The spatial detail of the predicted field profiles showed a larger degree of spontaneous emission noise induced aberration than is experimentally observed. This was explained in terms of the lack of temporal evolution in the FFT BPM model. However, the self-consistently predicted small signal gain of the amplifier showed excellent agreement with experimental data at the bias current levels for which the model successfully converged. Future work may show that an improved convergence procedure will allow the model to make accurate predictions over the entire range of bias currents used in practice.

In summary, the successful experimental evaluation of a fiber coupled MOPA system has been described. In addition, three successively more sophisticated numerical studies of MOPA system operation have been implemented and discussed and found to provide a helpful tool for understanding and predicting the behavior of these potentially important high power optical sources.

Bibliography

[1] T. Suzaki et al. 10 Gbit/s optical transmitter module with MQM DFB-LD and DMT driver IC. *Electronics Letters*, 26(2):151 - 152, January 1990.

[2] John G. Endriz et al. High power diode laser arrays. *IEEE Journal of Quantum Electronics*, 28(4):952 - 965, April 1992.

[3] Soichi Kobayashi and Tatsuya Kimura. Injection locking in AlGaAs semiconductor laser. *IEEE Journal of Quantum Electronics*, QE-17(5):681 - 689, May 1981.

[4] L. Goldberg and J. F. Weller. Injection-locked operation of a 20-element coupled-stripe laser array. *Electronics Letters*, 22(16):858–859, July 1986.

[5] L. Goldberg et al. Injection locking of coupled-stripe diode laser arrays. *Applied Physics Letters*, 46(3):236–238, February 1985.

[6] J. P. Hohimer et al. Single-channel injection locking of a diode-laser array with a cw dye laser. *Applied Physics Letters*, 47(12):1244–1246, December 1985.

[7] R. Wyatt et al. Megahertz linewidth from a 1.5 μm semiconductor laser with HeNe laser injection. *Electronics Letters*, 18(7):292–293, April 1982.

[8] H. L. Stover and W. H. Steier. Locking of laser oscillators by light injection. *Applied Physics Letters*, 8(4):91–93, February 1966.

[9] Robert Adler. A study of locking phenomena in oscillators. *Proceedings of the I.R.E. and Waves and Electrons*, 34:351–357, June 1946.

[10] Weng W. Chow. Injection locking of an index-guided semiconductor laser array. *IEEE Journal of Quantum Electronics*, QE-22(5):655–662, May 1986.

[11] Jean-Marc Verdiell et al. Analysis of injection-locked gain-guided diode laser arrays. *IEEE Journal of Quantum Electronics*, 27(3):396–401, March 1991.

[12] R. H. Pantell. The laser oscillator with an external signal. *Proceedings of the IEEE*, 53:474–477, May 1965.

[13] C. L. Tang and H. Statz. Phase-locking of laser oscillators by injected signal. *Journal of Applied Physics*, 38(1):323–324, January 1967.

[14] Weng W. Chow. Phase locking of lasers by injected signal. *Optics Letters*, 7(9):417–419, September 1982.

[15] Weng W. Chow. Theory of line narrowing and frequency selection in an injection locked laser. *IEEE Journal of Quantum Electronics*, QE-19(2):243–249, February 1983.

[16] G. C. Dente and M. L. Tilton. Modelling broad-area semiconductor optical amplifiers. 1991. To be published.

[17] Gregory L. Abbas et al. Injection behavior and modeling of 100mw broad area diode lasers. *IEEE Journal of Quantum Electronics*, 24(4):609–617, April 1988.

[18] Tadashi Saitoh and Takaaki Mukai. Gain saturation characteristics of traveling-wave semiconductor laser amplifiers in short optical pulse amplification. *IEEE Journal of Quantum Electronics*, 26(12):2086–2094, December 1990.

[19] A. A. M. Saleh. Nonlinear models of travelling-wave optical amplifiers. *Electronics Letters*, 24(14):835–837, July 1988.

[20] G. Ronald Hadley et al. Modeling of injection-locking phenomena in diode-laser arrays. *Optics Letters*, 11(3):144–146, March 1986.

[21] M. K. Chun et al. Injection-beam parameter optimization of an injection-locked diode-laser array. *Optics Letters*, 14(5):272–274, March 1989.

[22] Takaaki Mukai and Yoshihisa Yamamoto. Gain, frequency bandwidth and saturation output power of AlGaAs DH laser amplifiers. *IEEE Journal of Quantum Electronics*, QE-17(6):1028–1034, June 1981.

[23] M. J. O'Mahony. Semiconductor laser optical amplifiers for use in future fiber systems. *Journal of Lightwave Technology*, 6(4):531–544, April 1988.

[24] L. Goldberg et al. 12W broad area semiconductor amplifier with diffraction limited optical output. *Electronics Letters*, 27(11):927–929, May 1991.

[25] Lew Goldberg and J. F. Weller. Broad-area high-power semiconductor optical amplifier. *Applied Physics Letters*, 58(13):1357–1359, April 1991.

[26] N. A. Olsson et al. Semiconductor laser preamplifier. *Electronics Letters*, 24(9):569–570, April 1988.

[27] John R. Andrews. Travelling-wave samplifier made from a laser diode array. *Applied Physics Letters*, 48(20):1331–1333, May 1986.

[28] David Mehuys et al. Quasi-cw 3W diffraction-limited diode-to-diode optical amplifier. In *Conference on Lasers and Electro-Optics*, pages 224–225, 1992.

[29] Yoshihisa Yamamoto. Characteristics of AlGaAs Fabry-Perot cavity type laser amplifiers. *IEEE Journal of Quantum Electronics*, QE-16(10):1047–1052, October 1980.

[30] Gadi Eisenstein. Semiconductor optical amplifiers. *IEEE Circuits and Devices Magazine*, 25–30, July 1989.

[31] N. A. Olsson. Polarization-independent configuration optical amplifier. *Electronics Letters*, 24(17):1075–1076, August 1988.

[32] Lars Gillner et al. Semiconductor laser amplifier optimization: an analytical and experimental study. *IEEE Journal of Quantum Electronics*, 25(8):1822–1827, August 1989.

[33] L. Goldberg and J. F. Weller. Injection locking and single-mode fiber coupling of a 40-element laser diode array. *Applied Physics Letters*, 50(24):1713–1715, June 1987.

[34] L. Goldberg and M. K. Chun. Injection locking characteristics of a 1 W broad stripe laser diode. *Applied Physics Letters*, 53(20):1900–1902, November 1988.

[35] Donald M. Cornwell, Jr. et al. Phase-front measurementes of an injection-locked AlGaAs laser-diode array. *Optics Letters*, 14(17):910–912, September 1989.

[36] John R. Andrews and Gregory L. Schuster. High-power and high spatial-coherence broad-area power amplifier. *Optics Letters*, 16(12):913–915, June 1991.

[37] Jean-Pierre Weber and Shyh Wang. Analysis of the far-field output angle scanning by injection locking of a diode laser array. *Applied Physics Letters*, 48(25):1719–1721, June 1986.

[38] E. A. Swanson et al. High-speed electronic beam steering using injection locking of a laser-diode array. *Optics Letters*, 12(1):30–32, January 1987.

[39] Laurence R. Brewer. Suppression of beam steering in an injection-locked laser diode array. *Applied Physics Letters*, 59(24):3078–3080, December 1991.

[40] L. Y. Pang et al. Two-stage injection locking of high-power semiconductor arrays. *Optics Letters*, 15(13):728–730, July 1990.

[41] Soichi Kobayashi and Tatsuya Kimura. Optical phase modulation in an injection locked AlGaAs semiconductor laser. *IEEE Journal of Quantum Electronics*, QE-18(10):1662–1669, October 1982.

[42] Lew Goldberg et al. Frequency modulation characteristics of coupled stripe laser diode array. *IEEE Journal of Quantum Electronics*, QE-22(4):513–516, April 1986.

[43] Donald Mitchell Cornwell Jr. *Modulation Characteristics of a High-Power Semiconductor Master Oscillator Power Amplifier.* Master's thesis, University of Maryland at College Park, 1991.

[44] Olivier Lidoyne et al. Analysis of a homodyne receiver using an injection-locked semiconductor laser. *Journal of Lightwave Technology*, 9(5):659–665, May 1991.

[45] H. Nakajima and R. Derouiche. Direct demodulation of 140 mb/s fsk signals in an injection-locked multiquantum-well DFB laser. *IEEE Transactions Photonics Technology Letters*, 3(11):1029–1031, November 1991.

[46] M. Lucente et al. Coherent optical communication with injection-locked high-power semiconductor laser array. *Electronics Letters*, 25(17):1112–1114, June 1989.

[47] J. C. Livas et al. 1 Gbit/s injection-locked DPSK communications experiments for space applications. *Electronics Letters*, 27:123–125, 1991.

[48] Magdy M. Ibrahim. On injection locking of homogenously broadened lasers. *IEEE Journal of Quantum Electronics*, 14(3):145–147, March 1978.

[49] K. Otsuka. Coupled-wave theory regarding phase-locked-array lasers. *Electronics Letters*, 19(18):723–725, September 1983.

[50] J. K. Butler et al. Coupled-mode analysis of phase-locked injection laser arrays. *Applied Physics Letters*, 44(3):293–295, February 1984.

[51] E. Kapon et al. Supermode analysis of phase-locked arrays of semiconductor lasers. *Optics Letters*, 10(4):125–127, April 1984.

[52] Dan Botez and Donald E. Ackley. Phase-locked arrays of semiconductor diode lasers. *IEEE Circuits and Devices Magazine*, 8–16, January 1986.

[53] J. E. Epler et al. Supermodes of multiple-stripe quantum-well heterostructure laser diodes operated (cw, 300K) in an external-grating cavity. *Journal of Applied Physics*, 57(5):1489–1493, March 1985.

[54] J. E. Epler et al. Transverse modes of gain-guided coupled-stripe lasers: external cavity control of the emitter spacing. *Applied Physics Letters*, 47(1):7–9, July 1985.

[55] J. M. Verdiell et al. Array modes of multiple-stripe diode lasers: a broad-area mode coupling approach. *Journal of Applied Physics*, 66(3):1466– 1468, August 1989.

[56] J. M. Verdiell et al. A broad-area mode-coupling model for multiple-stripe semiconductor lasers. *IEEE Journal of Quantum Electronics*, 26(2):270–279, February 1990.

[57] G. Ronald Hadley et al. Comprehensive modeling of diode arrays and broad-area devices with applications to lateral index tailoring. *IEEE Journal of Quantum Electronics*, 24(11):2138–2152, November 1988.

[58] G. L. Abbas et al. Injection behavior of high-power broad-area diode lasers. *Optics Letters*, 12(8):605–607, August 1987.

[59] Anthony E. Siegman. *Lasers*. University Science Books, 1986.

[60] Govind P. Agrawal. Fast-fourier-transform based beam-propagation model for strip-geometry semiconductor lasers: inclusion of axial effects. *Journal of Applied Physics*, 56(11):3100–3109, December 1984.

[61] Govind P. Agrawal. Lateral-mode analysis of gain-guided and index-guided semiconductor-laser arrays. *Journal of Applied Physics*, 58(8):2922–2931, October 1985.

[62] G. R. Hadley et al. High-order ($\nu > 10$) eigenmodes in ten-stripe gain-guided diode laser arrays. *Applied Physics Letters*, 49(12):684–686, September 1986.

[63] G. Ronald Hadley et al. Free-running modes for gain-guided diode laser arrays. *IEEE Journal of Quantum Electronics*, QE-23(6):765–774, June 1987.

[64] M. D. Feit and J. A. Fleck Jr. Spectral approach to optical resonator theory. *Applied Optics*, 20(16):2843–2851, August 1981.

[65] Kazuo Shiraishi et al. Fiber-embedded in-line isolator. *Journal of Lightwave Technology*, 9(4):430–435, April 1991.

[66] Jerome K. Butler and Gary A. Evans. Analysis of double-heterostructure and quantum-well lasers using effective index techniques. *SPIE Laser Diode Technology and Applications*, 1043:148 –150, 1989.

[67] William Streifer and Eli Kapon. Application of the equivalent-index method to DH diode lasers. *Applied Optics*, 18(22):3724–3725, November 1979.

[68] Takanori Okoshi and Seiko Kitazawa. The Beam Propagation Method. In Eikichi Yamashita, editor, *Analysis Methods for Electromagnetic Wave Problems*, chapter 10, Artech House, 1990.

[69] J. Van Roey et al. Beam-propagation method: analysis and assessment. *Journal of the Optical Society of America*, 71(7):803–810, July 1981.

[70] G. P. Agrawal and N. K. Dutta. *Long-Wavelength Semiconductor Lasers*. Van Nostrand Reinhold Company, 1986.